(12) INTERNATIONAL APPLICATION PUBLISHED UNDER THE PATENT COOPERATION TREATY (PCT)

(19) **World Intellectual Property Organization**
International Bureau

(43) **International Publication Date**
**20 August 2026 (20.08.2026)**

WIPO | PCT

(10) **International Publication Number**
**WO 2026/174186 A1**

(51) **International Patent Classification:**
*C09K 19/58* (2006.01) *G02F 1/29* (2006.01)
*C09K 19/02* (2006.01) *G02F 1/135* (2006.01)
*G02F 1/133* (2006.01)

(21) **International Application Number:** PCT/US2026/015252

(22) **International Filing Date:** 13 February 2026 (13.02.2026)

(25) **Filing Language:** English

(26) **Publication Language:** English

(30) **Priority Data:**
63/758,760 14 February 2025 (14.02.2025) US

(71) **Applicant: THE REGENTS OF THE UNIVERSITY OF COLORADO, A BODY CORPORATE** [US/US]; 1800 Grant Street, 8th Floor, Denver, CO 80203 (US).

(72) **Inventors: SMALYUKH, Ivan, I.**; 1465 Ithaca Drive, Boulder, CO 80305 (US). **ZHAO, Hanqing**; 2040 Athens Street, Apartment E, Boulder, CO 80308 (US).

(74) **Agent: PILLOTE, Cynthia, L.**; Snell & Wilmer L.l.p., 1 East Washington Street, Suite 2700, Phoenix, AZ 85004-2556 (US).

(81) **Designated States** *(unless otherwise indicated, for every kind of national protection available)*: AE, AG, AL, AM, AO, AT, AU, AZ, BA, BB, BG, BH, BN, BR, BW, BY, BZ, CA, CH, CL, CN, CO, CR, CU, CV, CZ, DE, DJ, DK, DM, DO, DZ, EC, EE, EG, ES, FI, GB, GD, GE, GH, GM, GT, HN, HR, HU, ID, IL, IN, IQ, IR, IS, IT, JM, JO, JP, KE, KG, KH, KN, KP, KR, KW, KZ, LA, LC, LK, LR, LS, LU, LY, MA, MD, MG, MK, MN, MU, MW, MX, MY, MZ, NA, NG, NI, NO, NZ, OM, PA, PE, PG, PH, PL, PT, QA, RO, RS, RU, RW, SA, SC, SD, SE, SG, SK, SL, ST, SV, SY, TH, TJ, TM, TN, TR, TT, TZ, UA, UG, US, UY, UZ, VC, VN, WS, ZA, ZM, ZW.

(84) **Designated States** *(unless otherwise indicated, for every kind of regional protection available)*: ARIPO (BW, CV, GH, GM, KE, LR, LS, MU, MW, MZ, NA, RW, SC, SD, SL, ST, SZ, TZ, UG, ZM, ZW), Eurasian (AM, AZ, BY, KG, KZ, RU, TJ, TM), European (AL, AT, BE, BG, CH, CY, CZ, DE, DK, EE, ES, FI, FR, GB, GR, HR, HU, IE, IS, IT, LT, LU, LV, MC, ME, MK, MT, NL, NO, PL, PT, RO, RS, SE, SI, SK, SM, TR), OAPI (BF, BJ, CF, CG, CI, CM, GA, GN, GQ, GW, KM, ML, MR, NE, SN, TD, TG).

(54) **Title:** DISCRETE SPACE-TIME CRYSTAL DEVICE AND METHOD OF FORMING SAME

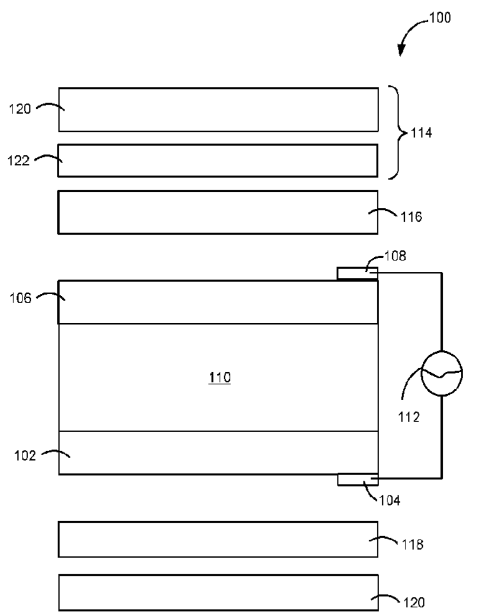


FIG. 1

(57) **Abstract:** Devices and system that exhibit both 1+1 dimensional (1 + ID) and 2+1 dimensional (2 + ID) discrete space-time crystals are disclosed. Exemplary devices include a first substrate, a second substrate, a doped chiral nematic liquid crystal material between the first substrate and the second substrate, and a power supply coupled to one or more of the first substrate and the second substrate, the power supply configured to apply an applied signal having a first period, wherein, in response to the applied signal, a period of an optical signal of light emitted from the device is an integer multiple of the first period. The doped chiral nematic liquid crystal material can include discrete space-time crystals.

WO 2026/174186 A1

[Continued on next page]

**Published:**

— *with international search report (Art. 21(3))*
— *before the expiration of the time limit for amending the claims and to be republished in the event of receipt of amendments (Rule 48.2(h))*

# DISCRETE SPACE-TIME CRYSTAL DEVICE AND METHOD OF FORMING SAME

## CROSS-REFERENCE TO RELATED APPLICATIONS

This application claims the benefit of U.S. Provisional Application No. 63/758,760, entitled DISCRETE SPACE-TIME CRYSTAL DEVICE AND METHOD OF FORMING SAME, and filed February 14, 2025, the contents of which are hereby incorporated herein by reference to the extent such contents do not conflict with the present disclosure.

## STATEMENT REGARDING FEDERALLY SPONSORED RESEARCH OR DEVELOPMENT

This invention was made with government support under grant number DE-SC0019293 awarded by the U.S. Department of Energy. The government has certain rights in the invention.

## FIELD OF INVENTION

The present disclosure generally relates to electronic devices. More particularly, examples of the disclosure relate to devices that exhibit discrete space-time properties.

## BACKGROUND OF THE DISCLOSURE

Time crystals have captured the interest of numerous researchers who are fascinated by the search of these new “crystals.” In analogy to the conventional space crystals, it has been suggested that time translation symmetry can be spontaneously broken in the lowest energy states of closed many-body systems, both in a quantum and classical manner. Unfortunately, a series of no-go theorems demonstrate that these closed systems are prohibited by nature at equilibrium. However, in non-equilibrium situations with Floquet external drives, it is possible to break time translation symmetry discretely, where the period of the driven system is an integer multiple of that of the external drive (the integer must be larger than one), resulting in what is called a discrete (Floquet) time crystal. The discrete time crystals were first observed in systems of nuclear spins and trapped ions, and recently many-body localization discrete time crystals were observed in quantum simulators and processors, which use the many-body localization to prevent the system from a thermalized fate. In addition to the many-body localization, discrete time crystals can be made to persist for a sufficiently long time by incorporating dissipation or introducing a prethermal state, which are also predicted for classical systems. While quantum mechanical time crystalline effects received a great deal of attention, their discovery in classical systems may be equally important from both fundamental and applied perspectives.

Any discussion of problems and solutions set forth in this section has been included in this disclosure solely for the purpose of providing a context for the present disclosure and should not be taken as an admission that any or all of the discussion was known at the time the invention was made or otherwise constitutes prior art.

## SUMMARY OF THE DISCLOSURE

Various embodiments of the present disclosure relate to classical discrete space-time crystals (DSTCs) in a chiral nematic liquid crystal (LC) system. Electrical switching of LCs is at the heart of the modern LC-enabled industries, including information displays and electro-optic devices; however, advantages of time-crystal emergence in these soft matter systems were never analyzed and have not been utilized. As set forth in more detail below, by applying a Floquet electrical signal to a chiral nematic LC sandwiched between parallel electrodes, both the spatial and temporal symmetries of emergent LC's structure revealed by optical images can be broken discretely and spontaneously, and the internal temporal periodicity of the system doubles in relation to the external drive. Both 1+1 dimensional (1 + 1D) and 2+1 dimensional (2 + 1D) discrete space-time crystals are observed, with the discrete time crystallization phases depending on temperature and external driving schemes, as illustrated by constructing a phase diagram. The rigidity (robustness) of the time crystals against temporal perturbation and spatial defects has been verified, with the DSTC phase maintaining order locally for a remarkably long time. Moreover, in analogy to defects in crystals, we also observe defects and their dynamics within the DSTCs.

In accordance with examples of the disclosure, a device includes a first substrate having a first electrical contact thereon, a second substrate having a second electrical contact thereon, a doped chiral nematic liquid crystal material between the first substrate and the second substrate, and a power supply coupled to one or more of the first electrical contact and the second electrical contact. The power supply can be configured to apply an applied signal having a first period, wherein, in response to the applied signal, a period of an optical signal of light emitted from the device is an integer multiple of the first period. In accordance with examples of these embodiments, the doped chiral nematic liquid crystal material comprises an ionic dopant. The ionic dopant can be or include a solvable ionic dopant that increases the electrical instability of the nematic liquid crystal material. The doped chiral nematic liquid crystal material can include greater than 0 and less than 0.2 wt% of the ionic dopant or greater than 0.05 wt% and less than 0.2 wt% of the ionic dopant.

In accordance with additional examples, a device includes a first substrate having a first electrical contact thereon, a second substrate having a second electrical contact thereon, a doped chiral nematic liquid crystal material between the first substrate and the second substrate, and a power supply coupled to one or more of the first electrical contact and the second electrical contact, the power supply configured to apply an applied signal having a first period, wherein the doped chiral nematic liquid crystal material comprises discrete space-time crystals. The doped chiral nematic liquid crystal material can include 1 + 1D discrete space-time crystals and/or 2 + 1D discrete space-time crystals.

In accordance with further examples of the disclosure, Pancharatnam–Berry phase gratings include a device as described herein. In accordance with additional examples, a Pancharatnam–Berry phase deflector includes a device as described herein.

In accordance with additional examples of the disclosure, an anti-counterfeiting system includes a device as described herein.

In accordance with yet additional embodiments, a method of producing discrete space-time crystals in a doped chiral nematic liquid crystal material includes providing a device as described herein and applying a Floquet electrical signal to one or more of the first or second electrical contacts.

These and other embodiments will become readily apparent to those skilled in the art from the following detailed description of certain embodiments having reference to the attached figures; the invention not being limited to any particular embodiment(s) disclosed.

## BRIEF DESCRIPTION OF THE DRAWING FIGURES

The patent or application file contains at least one drawing executed in color. Copies of this patent or patent application publication with color drawing(s) will be provided by the Office upon request and payment of the necessary fee.

A more complete understanding of exemplary embodiments of the present disclosure can be derived by referring to the detailed description and claims when considered in connection with the following illustrative figures.

FIG. 1 illustrates a device in accordance with examples of the disclosure.

FIG. 2 illustrates a Floquet sawtooth electrical signal applied to a device, where the temporal periodicity is $T\mathrm{E}$ = 0.5s and the amplitude (half of the peak to peak voltage) is $U\mathrm{max}$ = 50 V; inset images are captured by the camera within 2$T\mathrm{E}$ in accordance with examples of the disclosure.

FIG. 3 illustrates a schematic of the microscope-based experimental setup in accordance with examples of the disclosure.

FIG. 4 illustrates electrical signal magnitude and transmitted light intensity versus time for a single pulse in accordance with examples of the disclosure.

FIG. 5 illustrates time-zoom-in plot marked in FIG. 4 shows that the response time is about 2ms when the square pulse is switched on.

FIG. 6 illustrates numerically simulated electrical signal's magnitude and transmitted light intensity versus time corresponding to the relaxation process marked in FIG. 4; $T\mathrm{E}$ denotes the temporal periodicity of external drive for dynamic simulations.

FIG. 7 illustrates transmission versus time for a sawtooth electrical signal and for one-pulse waves.

FIG. 8 illustrates transmission versus time for a periodic sawtooth electrical signal within one $T\mathrm{E}$; the pattern emerges when the voltage is close to zero. The response time of the LC system for a sawtooth signal is on the same scale as $T\mathrm{E}$.

FIG. 9 illustrates polarizing optical micrograph (POM) with an inserted retardation plate showing a snapshot of a 1 + 1D DSTC.

FIG. 10 schematically illustrates how complex **n**(r) alters the polarization of light within different sample regions, resulting in varying polarized interference colors in accordance with examples of the disclosure.

FIG. 11 (a) and (b) illustrate **n**(**r**) in mid-planes (*x*-*y* planes) of the initial 2 states, which can be interpreted as containing a pair of -π and +π elementary domain-wall solitons, 3 as marked; (c) and (d) illustrate **n**(**r**) in vertical *x*-*z* planes marked in (a) and (b), respectively, shown in an inset of FIG. 11 (a) with cylinders colored according to the order parameter manifold, the sphere with diametrically opposite points identified; (e) and (f) illustrate experimental (e) and numerically simulated (f) three-photon excitation fluorescence polarizing microscopy images of two repeat units of a structure shown in (c), where polarizations of excitation light are marked by blue arrows; (g) and (h) illustrate experimental (g) and numerically simulated (h) POMs of the 2 + 1D DSTC (configuration 2); (i)-(k) illustrate **n**(**r**) (i) in mid-plane corresponding to the marked region in (h) and in *x-z* (j) and *y-z* (k) cross-sectional planes marked in (i). Scale bars are 10 µm in (g) and (h) and 5 µm in (e) and (f). Transmitting axes of polarizer and analyzer are marked by black double arrows; the slow axis of a retardation plate is marked by a green double arrow.

FIG. 12 (a) illustrates numerically simulated director field of 1 + 1D DSTC based on the Landau-de Gennes free energy functional, and the background is colored by the scalar order parameter *S* (right-side inset). The bottom inset schematically shows the many-body interactions among neighboring building blocks, which consist of topological solitons and disclinations; (b) illustrates Interaction energy per unit length (translation invariant along *y*) versus displacement relative to the equilibrium length (along *x*); (c) illustrates time-dependent director field showing the period-doubling phenomenon, with the selected region marked in (a); (d) and (e) illustrate enhanced contrast experimental (top) and numerically simulated (bottom) 1 POM images under a small (d) and large (e) electric field within one *T*E. (f) illustrates snapshots of S 2 distribution at different times within the selected region marked in (a); black dashed lines in 3 fixed positions are shown for reference; (g)-(i) illustrate snapshots of the director field (left) showing the topological transformation, angle *θ* of the disclination and the topological solitons in between vary smoothly when the voltage is close to zero. The corresponding schematics revealing their topological nature are shown on the right. Black circles show disclination cores; black dashed rings characterize director on closed loops. (j) illustrates external drive and twist angle *θ* of the disclination near the bottom surface within two external drive periods, *T*E. In the second TE, the structures are shifted by half of the spatial period. (k) illustrates director field profiles showing the transition from -1/2 to 10 +1/2 configurations of disclinations, which can be viewed as a Majorana-like quasiparticle and its antiparticle. The twist angle *θ*=cos-1(**τv**·**Ω**), where **τv** (blue arrow) is the tangent vector of the disclination (black cylinder) and **Ω** is the rotation vector (red arrow). (**l**) illustrates snapshots of the director field showing the transition after the voltage suddenly changes from +*U*max to -*U*max (left), followed by annihilation (middle) and generation (right) processes. (m)-(o) illustrate snapshots of the director field during the second *T*E (j), when topological solitons and disclinations shift by $L/2$ 16 compared to (g-i), respectively. Black dashed lines in (g)-(i), (m)-(o) show relative positions for reference.

FIG. 13 illustrates space-time image captured for the same time interval TE within the spatial region marked in FIG. 9.

FIG. 14 illustrates Fast Fourier transform (FFT) analysis of the video of 1 + 1D DSTC (left) and the electrical signals of external drive (right).

FIG. 15 illustrates 2 (a) POMs with retardation plate showing snapshots of the 2 + 1D DSTC of configurations disclosed herein. Right images are snapshots captured within $4TE$ as marked on the left, the black dots and dashed squares in the images serve as references. (d) illustrates trajectories tracking the center of each blue-colored region marked for the odd (green circle) and even (orange circle) drive period.

FIG. 16 illustrates average blue color signals versus time within the marked region in (j). a.u., arbitrary units.

FIG. 17 illustrates Individual (a) and average (b) displacements of trajectories in 15 (d) from odd (top) and even (bottom) spatial lattice lines, respectively.

FIG. 18 illustrates (a) phase diagram in coordinates of $T$E and the voltage amplitude $U$max for a sample of cell thickness $d$ = 5 μm at room temperature; (b) phase diagram as a function of the temperature and $U$max for the same sample as in (a) for $T$E = 0.5s; (c) phase diagram as a function of $T$E and $U$max for $d$ = 10 μm at room temperature; (d) phase diagram as a function of temperature and $U$max for the same sample as in (c) for $T$E = 0.5s. (e)-(i), POM snapshots of the time symmetry-unbroken phase (e), disordered phase (f), 1 + 1D DSTC phase (g), 2 + 1D DSTC phase (h) and co-existence phase (i), respectively. The helicoidal pitch is $p$ = 5 μm. Scale bars indicate 5 μm. Transmitting axes of polarizer and analyzer are marked by black double arrows; the slow axis of a retardation plate is marked by a green double arrow.

FIG. 19 illustrates (a) space-time image captured for the same time interval TE within a spatial stripe-like region showing the 1 + 1D DSTC "boil out" from a disordered state; (b) POM snapshots showing the 2 + 1D DSTC "boil out" from a disordered state (the elapsed time is marked on the panels; (c) POM snapshots showing the nucleation and growth of the DSTC region. The time interval of the two snapshots is 20 s (40 drives); (d), (e), POM snapshot (left) and space-time plot (right) of a 1 + 1D DSTC (d) and a disordered state (e) with temporal perturbation ΔTE randomly distribute within [-0.2$TE$, 0.2$TE$] (d) and [-0.4$TE$].

FIG. 20 illustrates (a) the emergence and disappearance of a defect region marked by a black dashed circle (elapsed times are marked on the panels); (b) recovery of 1 + 1D DSTC where a defect region is generated by a laser tweezer; (c) a quasi-dislocation with a missing row of “quasi-particles” within a strip region close to the transition phase (the POM snapshots are captured at elapsed times of $t = 0$ (left), $t = 10T_E$ (middle) and $t = 30T_E$ (right), respectively and the transmitting axes of the polarizer and analyzer are marked by black double arrows, the slow axes of the retardation plate are marked by green double arrows). Scale bars indicate 5 μm in (a), (c) and 20 μm in (b).

FIG. 21 illustrates (a) POM snapshots of neighboring odd (top) and even (bottom) drives at different times (scale bars indicate 3-10 μm); (b) positions of the topological quasiparticles in the middle of the selected region versus time for the same time interval of 0.5s, with positions marked atop of frames in (a).

FIG. 22 illustrates correlation function G(t) versus time for the same time interval $T_E$ = 0.5s. The fitting curve (black solid line) might be indicative of an exponential decay $e^{-t/\tau 0}$ with τ0 = 100s.

FIG. 23 illustrates (a) and (b) POM snapshots show an ordered quasi-hexagonal lattice (a) (marked with a white dashed hexagon) and a hexagonal lattice with a 5-7 defect pair; (b) (marked with a green pentagon and a yellow heptagon, respectively); (c) POM snapshots captured within $5T_E$, and the white dashed hexagons in the images serve for references. Although the images after a $3T_E$ look similar, they indeed differ slightly; (d) FFT analysis of the video of the fractional DSTC, where the peak is located around $0.3f/f_E$; (e) correlation function G(t) versus time for the same time interval $T_E$ = 0.5s, the 10$^{th}$ peak is located at $t = 33T_E$, and the 12$^{th}$ peak is located at $t = 40T_E$. Transmitting axes of the polarizer and analyzer are marked by white double arrows. Scale bars indicate 10 μm.

It will be appreciated that elements in the figures are illustrated for simplicity and clarity and have not necessarily been drawn to scale. For example, the dimensions of some of the elements in the figures may be exaggerated relative to other elements to help to improve the understanding of illustrated embodiments of the present disclosure.

DETAILED DESCRIPTION OF EXEMPLARY EMBODIMENTS

Although certain embodiments and examples are disclosed below and in the attached materials, it will be understood by those in the art that the invention extends beyond the specifically disclosed embodiments and/or uses of the invention and obvious modifications and equivalents thereof. Thus, it is intended that the scope of the invention disclosed should not be limited by the particular disclosed embodiments described below.

In this disclosure, any two numbers of a variable can constitute a workable range of the variable, and any ranges indicated may include or exclude the endpoints. Additionally, any values of variables indicated (regardless of whether they are indicated with about or not) may refer to precise values or approximate values and include equivalents, and may refer to average, median, representative, majority, or the like, in some embodiments. For example, the term about can refer to +/- 20, 10, 5, 2, or 1 percent of a value. Further, in this disclosure, the terms including, comprising, constituted by and having and their equivalents can refer independently to typically or broadly comprising, consisting essentially of, or consisting of in some embodiments. In accordance with aspects of the disclosure, any defined meanings of terms do not necessarily exclude ordinary and customary meanings of the terms.

As set forth in more detail below, various examples of the disclosure provide methods and devices that utilize 1+1-dimensional and 2+1-dimensional discrete space-time crystals in a liquid crystal system driven by a Floquet electrical signal. These classical time crystals comprise particle-like structural features and exist over a wide range of temperatures and electrical driving conditions. The phenomenon-enabling period-doubling effect in 1+1-dimensional discrete space-time crystals comes from their topological Majorana-like quasiparticle features, where periodic inter transformations of co-existing topological solitons and disclinations emerge in response to external stimuli and play pivotal roles. Exemplary discrete space-time crystals exhibit robustness against temporal perturbations and spatial defects. Our findings show that the simultaneous symmetry breaking in time and space can be a widespread occurrence in numerous open systems, not only in quantum but also in a classical soft matter context.

Electrical switching of liquid crystals (LCs) is at the heart of the modern LC-enabled industries, including information displays and electro-optic devices. By applying a Floquet electrical signal to a chiral nematic LC sandwiched between (e.g., parallel) electrodes, both the spatial and temporal symmetries of the emergent LC's structure revealed by optical images can be broken discretely and spontaneously, and the internal temporal periodicity of the system doubles in relation to the external drive. Both 1+1 dimensional (1 + 1D) and 2+1 dimensional (2 + 1D) discrete space-time crystals are observed, with the time crystallization phases depending on temperature and external driving parameters, as illustrated by constructing a phase diagram. Computer simulations demonstrate that the period-doubling effect is intimately related to the inter-transformations, generations, and annihilations of coexisting topological solitons and singular disclinations. The different states of these topological objects can be viewed as the particle and anti-particle states of the observed Majorana-like quasiparticles (a classical analogue of Majorana particles) forming our 1 + 1D space-time crystals. The rigidity (robustness) of the time crystals against temporal perturbation and spatial defects, with the discrete space-time crystals (DSTCs) phase maintaining order locally for a remarkably long time. Moreover, a candidate for a fractional discrete space-time crystal is observed when changing the sample 22 thickness. Our findings provide a new paradigm of time-crystalline LC meta matter, with technological utility.

FIG. 1 illustrates an exemplary device 100 in accordance with examples of the disclosure. Device 100 can be or be used to form any device noted herein.

Device 100 includes a first substrate 102 having a first electrical contact 104 thereon, a second substrate 106 having a second electrical contact 108 thereon, a doped chiral nematic liquid crystal material 110 between first substrate 102 and second substrate 106, and a power supply 112 coupled to one or more of first electrical contact 104 and second electrical contact 108, the power supply 112 configured to apply an applied signal having a first period. In accordance with aspects of these embodiments, in response to the applied signal, a period of an optical signal of light emitted from the device is an integer multiple of the first period. In accordance with additional or alternative aspects, the doped chiral nematic liquid crystal material comprises discrete space-time crystals. Device 100 can also include one or more of a polarized light source 114, a condenser 116, a retardation plate 118, and/or an analyzer 120.

First substrate 102 and/or second substrate 106 can be formed of any suitable material. For example, first substrate 102 and/or second substrate 106 can be formed of transparent material, such as glass. Particular examples of transparent substrate material include glass, indium tin oxide (ITO) glass, soda-lime glass, or the like.

First electrical contact 104 and/or second electrical contact 108 can be formed of any suitable conductive material. For example, first electrical contact 104 and/or second electrical contact 108 can be formed of a metal, such as tin-based solder.

Doped chiral nematic liquid crystal material 110 can be any suitable doped chiral nematic liquid crystal material that exhibits discrete space-time crystal as described herein. In accordance with examples, the doped chiral nematic liquid crystal material comprises 1 + 1D discrete space-time crystals. In accordance with further examples, the doped chiral nematic liquid crystal material comprises 2 + 1D discrete space-time crystals. In accordance with yet further examples, the doped chiral nematic liquid crystal material comprises one or more of 5CB(4-Cyano-4'-pentylbiphenyl) and E7 (a mixture of 4-Cyano-4'-pentylbiphenyl, 4′-Heptyl-4-biphenylcarbonitrile, 4′-Octyloxy-4-biphenylcarbonitrile or 4-Cyano-4′-Pentylterphenyl). In accordance with further examples, the doped chiral nematic liquid crystal material comprises an ionic dopant. The ionic dopant can be, for example, a solvable ionic dopant that increases the electrical instability of the nematic liquid crystal material. By way of particular examples, the ionic dopant can be or include cetyltrimethylammonium bromide, other cetyl alkyl ammonium compounds, or the like. The doped chiral nematic liquid crystal material can include greater than 0 and less than 0.2 wt% of the ionic dopant or greater than 0.05 wt% and less than 0.2 wt% of the ionic dopant.

Power supply 112 can be or include any suitable power supply. In accordance with examples, power supply 112 is or includes a Floquet electrical signal source. Power supply 112 can be configured to apply an applied signal having a first period.

Polarized light source 114 can include any suitable polarized light source. For example, polarized light source 114 can be or include a light source 120 and a polarizer 122 disposed between light source 114 and first substrate 102. Light source 120 can be or include, for example, LED light source. Polarized light source 114 can suitably be proximate first substrate 102.

Retardation plate 118 can be or include, for example, a first-order full-wave retardation plate .

Analyzer 120 can be used to analyze a signal or to use a signal for various applications, such as applications noted herein. For example, analyzer 120 can be configured to receive a signal from a linear polarizing film.

Specific Examples

The examples provided below are meant to be illustrative and not restrictive. Unless otherwise noted, the disclosure is not limited to the specific examples provided below.

A sample is prepared by sandwiching a chiral nematic LC between two electrically conductive transparent substrates (e.g., substrates 102, 106), where the LC is doped with ionic substances or an ionic dopant. In response to a Floquet electrical signal (e.g., as shown in FIG. 2), the confined LC can spontaneously form spatially periodic configurations, which can be captured by a camera of an optical microscope system (e.g., analyzer 120) or using the system illustrated in FIG. 3.. The spatially varying optical phase retardation pattern is produced by the LC with complex structure of director orientation driven by the field, which can be vividly revealed by inserting an additional first-order full-wave retardation plate (e.g., retardation plate 116, FIGS. 1 and 3). The alternating blue and purple spatial regions shown in FIG. 2 indicate spatial variations in the LC's three-dimensional 10 (3D) structures represented by the locally averaged molecular orientation direction n (dubbed the "director").

Because the exemplary system includes a chiral nematic LC with ion doping under surface confinement with perpendicular boundary conditions, which is incompatible with the uniform twist of the chiral nematic phase, it is important to examine its response to different electrical signals. Using the experimental setup shown in FIG. 3, one can measure the light transmission over a relatively large area (~1 $mm^2$) captured by the detector. The system responds within a few milliseconds after turning the voltage on, as shown in FIGS. 4 and 5, whereas the relaxation back to the initial state is a slower process when the voltage is turned off, as shown in FIGS. 4 and 6. As different sawtooth electrical signals are applied, complex responses (FIGS. 7 and 8), where the relaxation process occurs on the timescales of ~0.1-1s occur. These temporal responses are generally consistent with the timescales of the complex space-time configurations, driving rich dynamic phenomena discussed below.

The polarized light interference pattern exhibits clear spatial periodicity under Floquet sawtooth electrical signal, as shown in FIGS. 6 and 8, which can be reproduced by numerical simulations of the director configurations based on both Frank-Oseen and Landau-de Gennes free energy models (FIGS. 11 and 12) and the subsequent modelling of polarized light propagation through such a system with the Jones-matrix method. While the spatiotemporal crystallization in light polarization (and its color) patterns is apparent from imaging, it also reveals similar behavior in the spatiotemporal response of the chiral nematic LC medium. By analyzing the interference-color signal within the camera-captured micrographs of these regions over time (FIG. 13), we find that the spatial pattern recurs every two periods of the external Floquet drive (FIG. 14). This behavior is often called the "period-doubling" phenomenon, indicating that the time translation symmetry is broken discretely. The near-neighbor correlations are antiferromagnetic-like both in time and in space, similar to the case of previous theoretical studies for different systems. Furthermore, the discrete time crystallization phase can be observed for different chemical chiral LC substances. Three distinct configurations have been identified as the 2 + 1D DSTCs (FIG. 15). Notably, configuration 1 (FIG. 15 (a)) and configuration 2 (FIG. 15 (b) and FIG. 16) are observed under the same conditions, while configuration 3 (FIG. 15 (c)) is typically observed only for higher $d/p$ ratios, where $d$ is the cell thickness and $p$ is the helicoidal pitch of the chiral nematic LC. Although these three configurations of 2 + 1D classical discrete time crystals can have different spatial lattice periodicities that are comparable to the helicoidal pitch, along the temporal axis they feature the period-doubled response to the external drive (FIG. 15 (a)-(c)). To characterize the period-doubling phenomenon within long times, we track the colored regions, which correspond to different localized structures of director field $\mathbf{n}(\mathbf{r})$. FIG. 15 (d) shows positions-vs-time trajectories of the center of the blue regions, overlaid on top of the images, revealing that these regions in odd/even lines of the lattice move in opposite directions within each drive period (anti-ferromagnetic-like), which is also evident by tracking the average blue signals (FIG. 16). Furthermore, the individual (FIG. 17 (a)) and collective spatial displacements (FIG. 17(b)) take place while maintaining the period-doubling behavior.

**Majorana-like quasi-particle nature of building blocks of time crystals.** Our computer simulations based on the Ginzburg-Landau equation accounting for dielectric, flexoelectric, and screening-charge effects reproduce the experimental observations of the sample's nonsingular initial state at zero field, as well as the topological quasiparticles and the period-doubling phenomenon in the DSTC states with both nonsingular domain wall solitons and singular line defects (FIG. 12). When the initial state (FIG. 11) transforms into the 1 + 1D DSTC state (FIG. 12), the symmetry breaking becomes different during the time crystal formation over tens of electrical driving periods. This transition takes place while complying with the sample's perpendicular boundary conditions for $\mathbf{n}(\mathbf{r})$ on confining substrates. The period-doubling phenomenon within the 1 + 1D DSTC is directly observed in the snapshots of the director field and the scalar order parameter's spatial distribution (FIG. 12(c) and (f)). To understand the underlying mechanism, we thoroughly analyzed the dynamic process, finding the inter-transformations, generations, and annihilations of coexisting topological solitons and singular disclinations (FIG. 12 (g)-(o)). The singular disclination structures, as well as the fragments of solitonic nonsingular walls between them, are the building blocks of the 1 + 1D time crystal, which can be treated as Majorana-like quasiparticles and respective anti-particles (FIG. 12 (k)), because the studied disclination profiles in their cross-sections smoothly transform as spinors following the Majorana equation. The solitonic walls exhibit temporal evolutions that comply with the transformations of the singular line defects at their ends (FIG. 12 (g)-(i)).

In the time crystal phase, the particle-antiparticle inter-transformation occurs when the external voltage $U$ smoothly changes from negative to positive (FIG. 12 (g)-(j)). The director field around the translationally invariant disclination line region can be quantified by the characteristic twist angle $\theta$ ($\theta \in [0, \pi]$), whereas the core (center) of the disclination line is a singularity in **n**(**r**), within which the director orientations cannot be defined. When the amplitude of instantaneous negative voltage $U$ is relatively large, $\theta$ equals π for the top and 0 for the bottom disclinations (FIG. 12(g)), respectively, which means that **n**(**r**) confined to the plane perpendicular to disclination lines (with the effective order parameter space being $\mathbb{S}^1/\mathbb{Z}_2$, the one sphere – or circle - with diametrically opposite points identified, for the director confined to the cross-sections). These defect lines can be referred to as wedge disclinations with winding numbers −1/2 and +1/2 defined in the two-dimensional cross-sections orthogonal to the defect lines (FIG. 12 (j)), respectively. The 2D winding numbers ±1/2 of disclinations relate to the accumulated angle of **n**(r) rotation as one circumnavigates the disclination core once, divided by 360°, with the positive sign corresponding to the counterclockwise rotation, matching that of circumnavigation, and negative sign referring to the clockwise case. However, once the director is allowed to rotate out of the 2D plane orthogonal to the defect lines, becoming 3D in nature, the initial −1/2 and +1/2 structures become topologically the same. While the −1/2 and +1/2 cross-sectional structures would correspond to topologically distinct defect states in a purely 2D system, they are topologically analogous and deformable to one another in our system because 3D rotations of director are allowed. Indeed, these structures morph one to another over time via smooth director rotations (FIG. 12 (g)-(i)), so that they can be treated as Majorana-like quasiparticles and respective anti-quasiparticles. These defect lines within our LC's 3D space are the topologically nontrivial elements of the first homotopy group $\pi_1(\mathbb{S}^2/\mathbb{Z}_2)=\mathbb{Z}_2$, where $\pi_1$ refers to the measuring circle around the defect line and the director's order parameter space is $\mathbb{S}^2/\mathbb{Z}_2$, the two-sphere with diametrically opposite points identified. Between the two disclination regions, the −π-rotation Néel domain wall solitons (with +/− defined by counterclockwise/clockwise rotation when traversing the topological soliton from left to right) are spatially embedded (FIG. 12 (g)). The domain wall solitons are also labelled as elements of the first homotopy group, $\pi_1(\mathbb{S}^2/\mathbb{Z}_2)=\mathbb{Z}_2$, and are also allowed to smoothly inter-transform to have 2D cross-sections of different types (Néel or Bloch type) while here being terminated by the two disclination lines. Thus, both singular and solitonic $\pi_1(\mathbb{S}^2/\mathbb{Z}_2)=\mathbb{Z}_2$ structures morph between geometrically different but topologically the same states under electric driving—akin to deforming a donut into a coffee mug without changing the topological properties (FIG. 12 (g)-(i)). As the voltage $U$ increases from negative values to zero (FIG. 12 (h)), the angle $\theta$ characterizing both wall-terminating disclinations smoothly changes to π/2 (corresponding to pure twist winding), and the initial −π-rotation Néel domain wall solitons (with bend-splay structures) transform to Bloch domain wall solitons (with pure twist structures). As the voltage $U$ further increases to $U > 0$ (FIG. 12 (i)), $\theta$ changes to 0 for the top and π for the bottom defect lines, and the Bloch domain wall solitons transform to the +π-rotation Néel domain wall solitons. The transition is continuous during the linear voltage change, and the positions of the disclinations and solitons do not shift spatially, just morph geometrically. The array of topological quasiparticles formed by solitonic walls terminated on singular defect lines maintains its topological nature (FIG. 12 (i)) until $U$ suddenly changes from the positive maximum value to the negative maximum value (FIG. 12 (l)), at which point topological particle-antiparticle pairs annihilate and re-generate, while the locations of the emerged quasiparticles are found synchronously shifted by half a spatial period ($L/2$) away from the previous ones. The origin of quasiparticles' annihilation and regeneration refers to the discontinuity of external drive: the voltage changes dramatically, but the director field cannot deform correspondingly fast. After the generation, compared to the structures of the director field one temporal period ($T$E) before (FIG. 12 (g)-(i) and (m)-(o)), the disclinations and topological solitons are the same, with an $L/2$ shift, so that the system adopts the exact same configuration every 2$T$E, resulting in the period-doubling phenomenon. In the experiments and simulations alike (FIG. 12 (d) and (e)), even when the optical images appear almost homogeneously dark under a high electric field between crossed polarizers, the defects and director deformations do not fully disappear, as evident from the enhanced contrast POM images that reveal effective "memory" of the periodic deformations that allows for correlating positions of these topological objects within 2*T*E. Serving as building blocks of time crystals, the self-free energy of a quasiparticle unit (FIG. 12 (a), including a pair of Majorana-like singular defect quasiparticles and domain wall solitons in-between them) relative to the ground state in a passive LC is ~ $1.3\times10^3$ *k*B*T*/μm (*k*B is the Boltzmann constant and *T* is the temperature), as the system is powered by the external drive to overcome the energy gap, consistent with the anticipated existence of Majorana-like quasiparticles in active and driven nematic LC systems out of equilibrium. Moreover, the elasticity-mediated energy of the interaction between neighboring units is ~10 *k*B*T* with a 10% compression or stretching calculated from Landau–de Gennes free energy (FIG. 12 (b)), further indicating that these topological quasiparticles behave as particle-like objects, which can collectively form a crystal. In addition to reproducing the topological time-crystalline character, by changing the voltage amplitude in the computer simulations, the Fourier analysis of the time-dependent **n**(**r**,t) reveals the transitions of period-doubling time-crystalline states to other dynamic states, which are consistent with experimental results.

**Stability and robustness.** The stability range of emergent phase of discrete time crystallization depends on the cell thickness, LC's helicoidal pitch, temperature, voltage amplitude *U*max, and external drive period *T*E. To construct the phase diagram, we employ samples of different cell thickness but the same LC pitch while controlling temperature, *U*max, and *T*E (FIG. 5(a)-(d)). We find five distinct phases (FIG. 18 (e)-(i)) within explored ranges of these parameters: a time-symmetry-unbroken phase (FIG. 18 (e)) with the temporal periodicity of LC system being the same as the external drive, a disordered phase (FIG. 18 (f)) with a disordered response to the external drive, and a phase co-existence region (FIG. 18 (i)), where both the 1 + 1D DSTC (FIG. 18 (g)) and 2 + 1D DSTC (FIG. 18 (h)) phases can co-exist. For a thin cell, we observe both the 1 + 1D and 2 + 1D DSTC phases depending on *T*E (ranging from 0.35s to 1s) and temperature (ranging from 24 °C to 31 °C). This indicates that the DSTC is quite robust within a broad range of parameters as the maximum drive period can be ~ 3 times longer than the minimum one, whereas the intrinsic elastic and dielectric properties of the LC can undergo a ~40% change with such temperature variations correlating with changes of the LC's scalar order parameter. The temporal range of *T*E in DSTC phases is on the same timescale as the response time of chiral LCs to a sawtooth electrical signal (FIGS. 7 and 8),which further demonstrates the importance of the coupling between the electrical drive and the LC director field that is structurally complex even in its initial state at no applied voltages (FIG. 11). Interestingly, the phase diagrams in the coordinates of temperature and $T_E$ exhibit an unexpected resemblance: increasing the temperature yields behavior similar to that of decreasing $T_E$. This is because when $T_E$ is small, the director field fails to maintain its topological structure as the external electric field changes too rapidly; similarly, as the temperature increases, the elastic and dielectric constants decrease, decreasing the interaction energy between the quasiparticles, so the system cannot maintain its topological structure either. For a thick cell, the DSTC phase also exists over a broad range. We examined the rigidity (robustness) of the DSTC starting from its formation, where the DSTC spontaneously "boils out" from the disordered state (FIG. 18 (a) and (b)), resembling previous theoretical findings, which indicates the spontaneous symmetry breaking both in space and time. Within the DSTC phase, the DSTC region grows as the disordered region shrinks (FIG. 19 (c)) because the disordered state is "unstable" relative to the ordered configuration. We further examine the rigidity by adding random temporal perturbations $\Delta T_E$ to the external drive period at each period, finding that both the 1 + 1D and 2 + 1D DSTC phases are robust under such temporal perturbations (FIG. 19 (d) and (e)). The spontaneous symmetry breaking both in space and time and robustness against temporal perturbations are important properties of space-time crystals, serving as verification criteria of space-time crystals that our system appears to satisfy.

**Lattice defects and long-range order.** Just like conventional space crystals often have defects, various crystal lattice imperfections (like dislocations, vacancies and self-interstitial points) can emerge in DSTCs (FIG. 20). However, because of the rigidity of the time crystals, the discrete space-time crystallization phase tends to recover from such lattice imperfections after tens of drives (FIG. 20 (a)). Additionally, lattice defects can be introduced by manipulating the LC with a focused infrared beam of laser tweezers. The laser beam forms defects in space coordinates of the DSTC, which also tend to disappear with time (FIG. 20 (b)). These results motivate us to experimentally measure how long our classical DSTC (FIG. 21) can show the period-doubling phenomenon, revealing that the 2 + 1D DSTCs maintain period-doubling locally (within the camera captured region) for hours (~104 drives) and the 1 + 1D DSTCs for about 24 hours (~105 drives). To verify the local temporal correlation, we define the temporal correlation function $G(t) = \langle\Phi(t)\Phi(0)\rangle-\langle\Phi(t)\rangle\langle\Phi(0)\rangle$, where the brackets indicate an average and $\Phi$ is the signals captured by the camera. It's well-known that for a smectic phase, the spatial correlation function 10 $G(r)$ decays in a power-law manner depending on the distance $r$, where the power-law index should be small. Interestingly, an exponential decay (FIG. 21) on t could fit the temporal correlation function of 1 + 1D DSTC, with both the spatial and temporal fluctuations tending to eventually destroy the corresponding correlation in the long ranges. Achieving extended correlations therefore generally includes enhancing system controls that preclude issues like thermally- or vibrations-induced drift. Numerically, by introducing a white-noise stochastic perturbation $f_{noise}(t)$, with an autocorrelation $\langle f_{noise}(t) f_{noise}(t')\rangle = 2\eta_0 T_{eff}\delta(t-t')$ (where $\eta_0$ is the friction coefficient and $T_{eff}$ is the effective temperature of the thermal perturbation), we observe that the order of the system decreases dramatically as the effective temperature increases. More defects emerge in the bulk, and the lifetime (correlation time) decreases exponentially with increasing $T_{eff}$, suggesting a (thermally) activated time crystal. Under conditions around the phase transition 22 (FIG. 18), the lifetime of the DSTC can be very short due to frequent occurrences of line dislocations (FIG. 20 (c)), causing emergence of the disordered states within only ten-to-hundred drives.

**Candidates of fractional discrete time crystals.** The emergent spatiotemporal response of chiral nematic LCs under the Floquet drive can give origins to plentiful other phenomena, such as the quasi-hexagonal lattices seen in the spatial coordinates (FIG. 23 (a)) when $d/p > 3$, which potentially can be a fractional discrete time crystal (FIG. 23). The intrinsic time periodicity is not an integer multiple of the external drive (FIG. 23 (c)), and the FFT analysis (FIG. 23 (d)) reveals a peak around $10T_E/3$ ($f \approx 0.3f_E$). The strong noise around the peak in FFT analysis originates from the emergence of lattice imperfections (such as 5-7 defects, FIG. 23 (b)) in spatial coordinates. We observe lattice imperfections within a region of ~10 hexagonal units over 200 external drives. In addition, the temporal correlation function (FIG. 23 (e)) further suggests the internal temporal period is approximately $33T_E/10$ or $10T_E/3$ ($40T_E/12$). Interestingly, fractional discrete time crystals of similar fractional numbers (~3.3 and 100/29) have been observed in two different quantum systems. Whether they share common universal mechanisms remains an open question.

As noted above, observations of classical discrete space-time crystals reveal the generality of time crystallization dynamics. In our classical LC-based discrete space-time crystals, the time symmetry is discretely broken while being accompanied with space symmetry breaking, yielding 1 + 1D and 2 + 1D space-20 time crystals. These DSTCs can be described as comprising arrays of spatially and temporarily localized quasiparticles interacting with each other within the overall out-of-equilibrium setting (FIG. 12 (a) and (b)) observed experimentally. These classical DSTCs may offer a new route to creating various forms of meta matter, where the basic building blocks are localized not only in space, but also in time, as well as have the emergent topological nature. They may allow designing spatially or temporally localized structures as versatile reconfigurable beam deflectors, steerers, and lasing elements. The examined rigidity of our classical DSTC allows for maintaining order locally over times much longer than the discrete time crystals in quantum systems, which is because, although the classical system cannot enjoy the benefits of many-body localization, there is no quantum coherence, and the relative noise from thermal fluctuations is much smaller for soft matter systems when considering the system's internal elasticity-mediated interactions.

The example embodiments of the disclosure described above do not limit the scope of the invention, since these embodiments are merely examples of the embodiments of the invention. Any equivalent embodiments are intended to be within the scope of this invention. Indeed, various modifications of the disclosure, in addition to the embodiments shown and described herein, such as alternative useful combinations of the elements described, may become apparent to those skilled in the art from the description. Such modifications and embodiments are also intended to fall within the scope of the appended claims.

CLAIMS:

1. A device comprising:

a first substrate having a first electrical contact thereon;

a second substrate having a second electrical contact thereon;

a doped chiral nematic liquid crystal material between the first substrate and the second substrate; and

a power supply coupled to one or more of the first electrical contact and the second electrical contact, the power supply configured to apply an applied signal having a first period,

wherein, in response to the applied signal, a period of an optical signal of light emitted from the device is an integer multiple of the first period.

2. The device of claim 1, wherein the doped chiral nematic liquid crystal material comprises one or more of 5CB(4-Cyano-4'-pentylbiphenyl) and E7 (a mixture of 4-Cyano-4'-pentylbiphenyl, 4’-Heptyl-4-biphenylcarbonitrile, 4’-Octyloxy-4-biphenylcarbonitrile and 4-Cyano-4’-Pentylterphenyl).

3. The device of claim 2, wherein the doped chiral nematic liquid crystal material comprises an ionic dopant.

4. The device of claim 3, wherein the ionic dopant comprises a solvable ionic dopant that increases the electrical instability of the nematic liquid crystal material.

5. The device of claim 3, wherein the ionic dopant comprises cetyltrimethylammonium bromide.

6. The device of claim 3, wherein the doped chiral nematic liquid crystal material comprises greater than 0 and less than 0.2 wt% of the ionic dopant.

7. The device of claim 3, wherein the doped chiral nematic liquid crystal material comprises greater than 0.05 wt% and less than 0.2 wt% of the ionic dopant.

8. The device of claim 1, further comprising a polarized light source proximate the first substrate.

9. The device of claim 1, wherein the power supply comprises a Floquet electrical signal source.

10. A device comprising:

a first substrate having a first electrical contact thereon;

a second substrate having a second electrical contact thereon;

a doped chiral nematic liquid crystal material between the first substrate and the second substrate; and

a power supply coupled to one or more of the first electrical contact and the second electrical contact, the power supply configured to apply an applied signal having a first period,

wherein the doped chiral nematic liquid crystal material comprises discrete space-time crystals.

11. The device of claim 10, wherein the doped chiral nematic liquid crystal material comprises 1 + 1D discrete space-time crystals.

12. The device of claim 10, wherein the doped chiral nematic liquid crystal material comprises 2 + 1D discrete space-time crystals.

13. The device of claim 10, wherein the doped chiral nematic liquid crystal material comprises one or more of 5CB(4-Cyano-4'-pentylbiphenyl) and E7 (a mixture of 4-Cyano-4'-pentylbiphenyl, 4′-Heptyl-4-biphenylcarbonitrile, 4′-Octyloxy-4-biphenylcarbonitrile and 4-Cyano-4′-Pentylterphenyl).

14. The device of claim 10, wherein the doped chiral nematic liquid crystal material comprises an ionic dopant.

15. The device of claim 3, wherein the ionic dopant comprises a solvable ionic dopant that increases the electrical instability of the nematic liquid crystal material.

16. The device of claim 14, wherein the doped chiral nematic liquid crystal material comprises greater than 0 and less than 0.2 wt% of the ionic dopant.

17. Pancharatnam–Berry phase gratings comprising the device of any of claims 1-16.

18. A Pancharatnam–Berry phase deflector comprising the device of any of claims 1-16.

19. An anti-counterfeiting system comprising the device of any of claims 1-16.

20. A method of producing discrete space-time crystals in a doped chiral nematic liquid crystal material, the method comprising:

providing a device as set forth in any of claims 1-16; and

applying a Floquet electrical signal to one or more of the first or second electrical contacts.

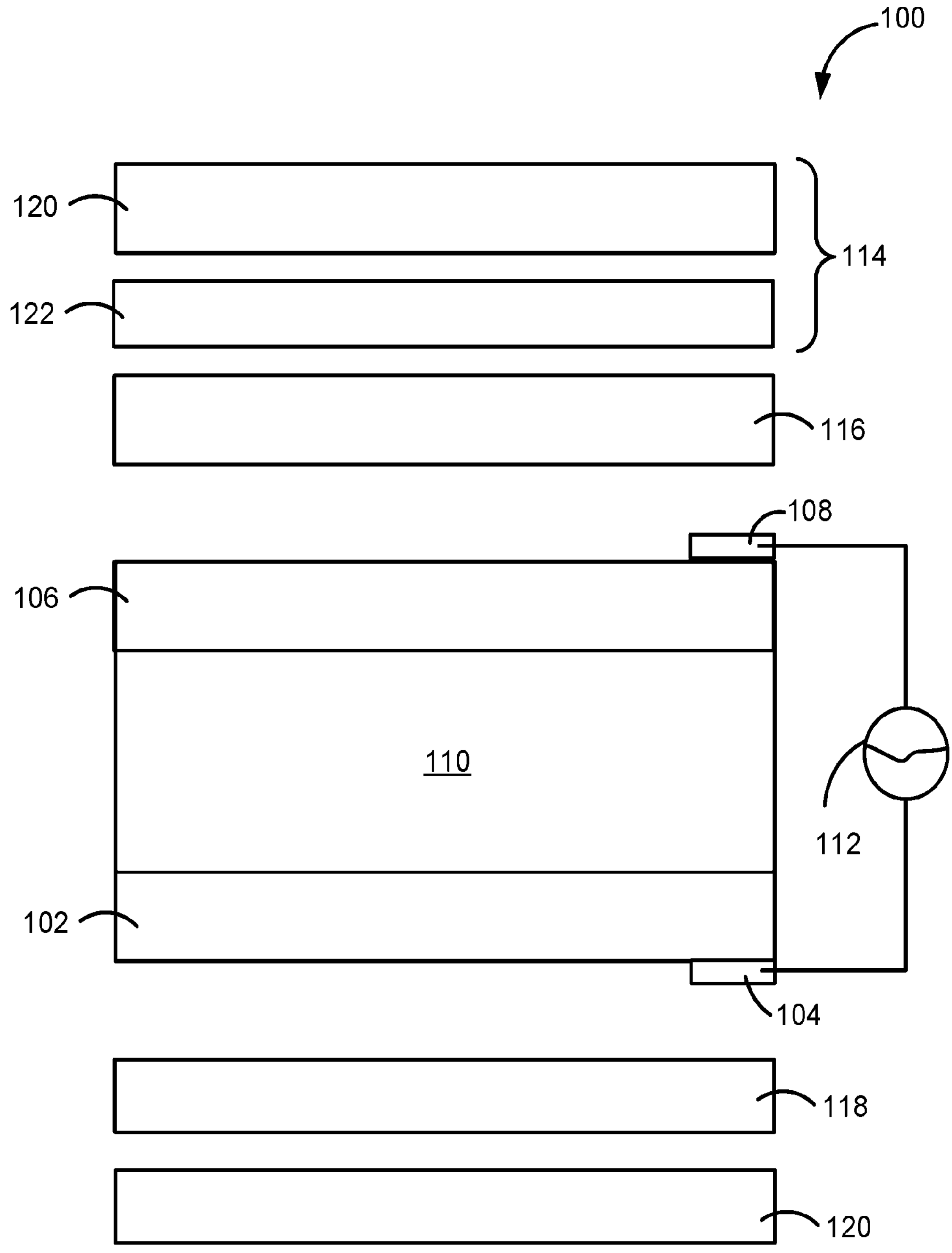


FIG. 1

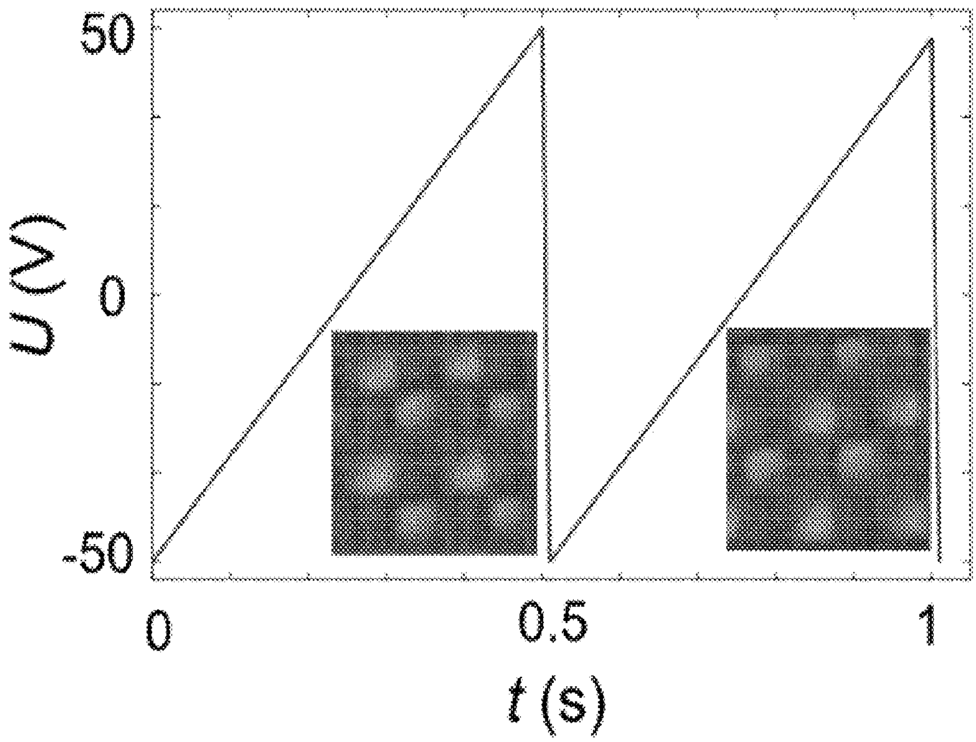


FIG. 2

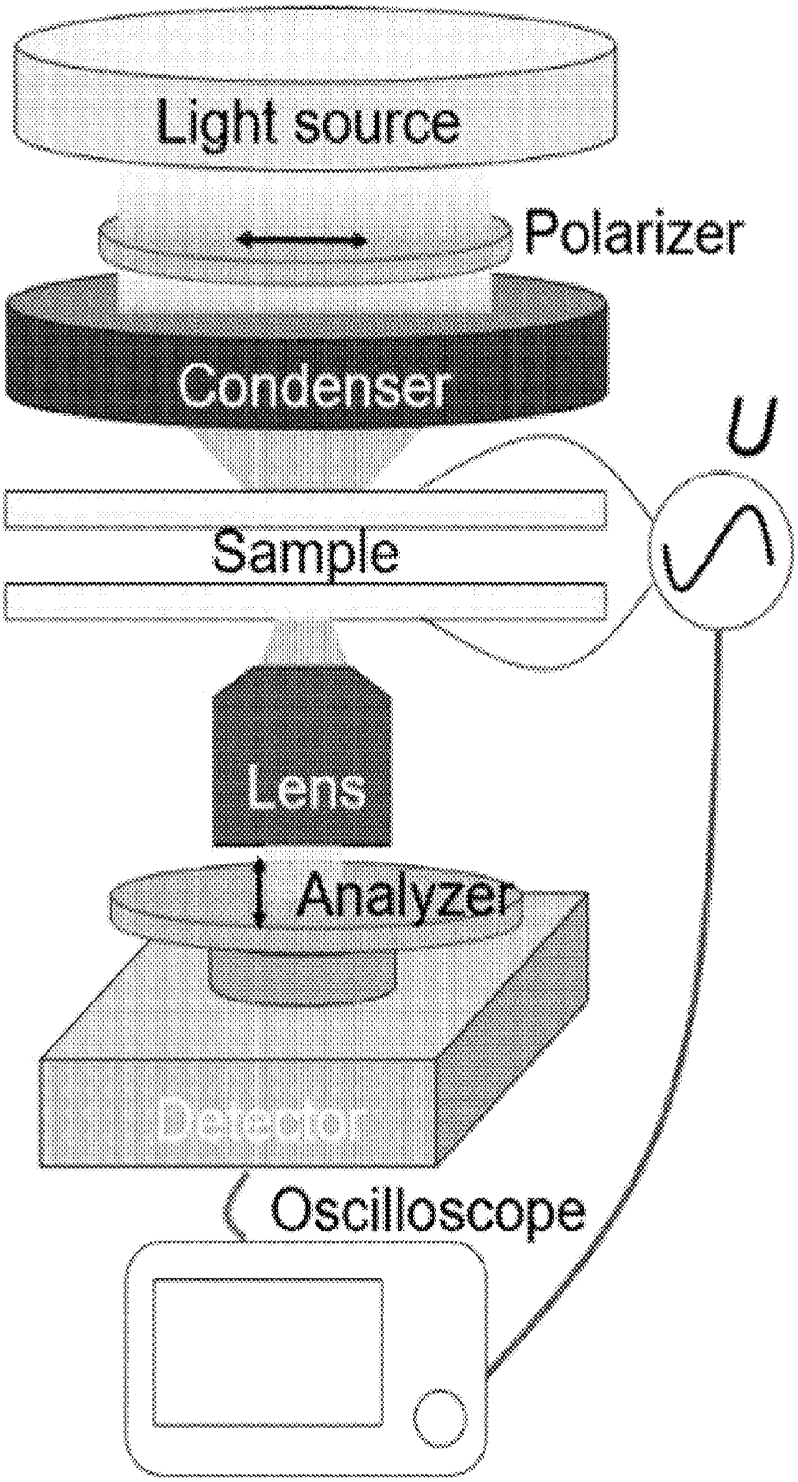
Light source
Polarizer
Condenser
U
Sample
Lens
Analyzer
Detector
Oscilloscope

FIG. 3

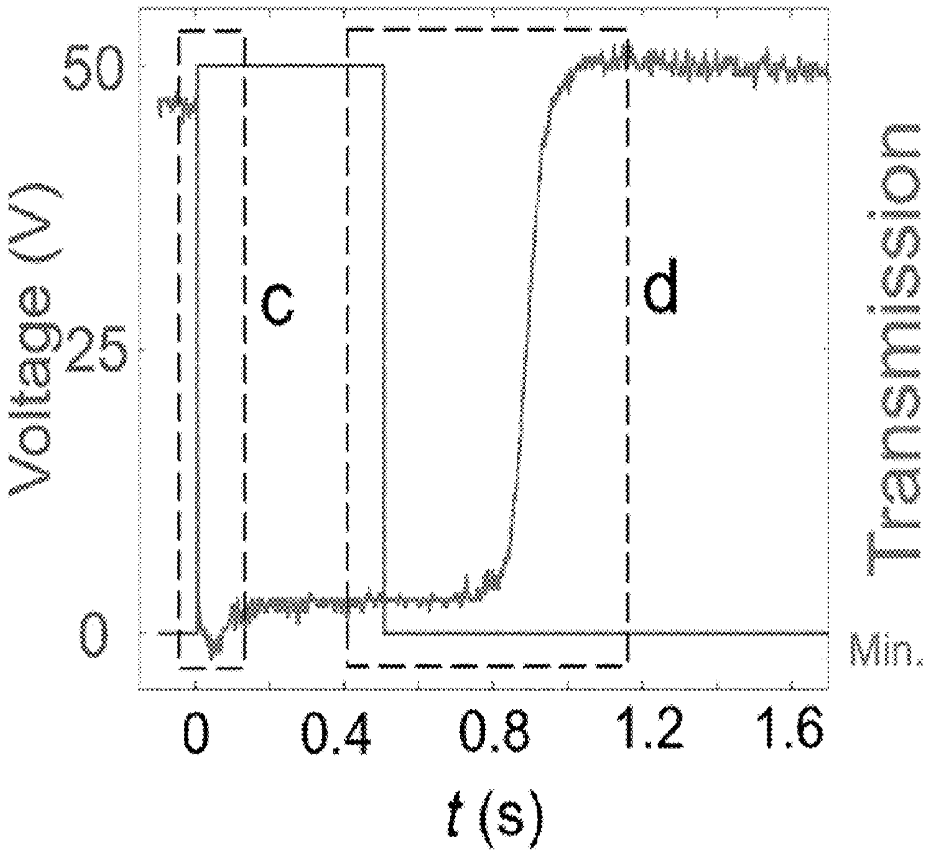


FIG. 4

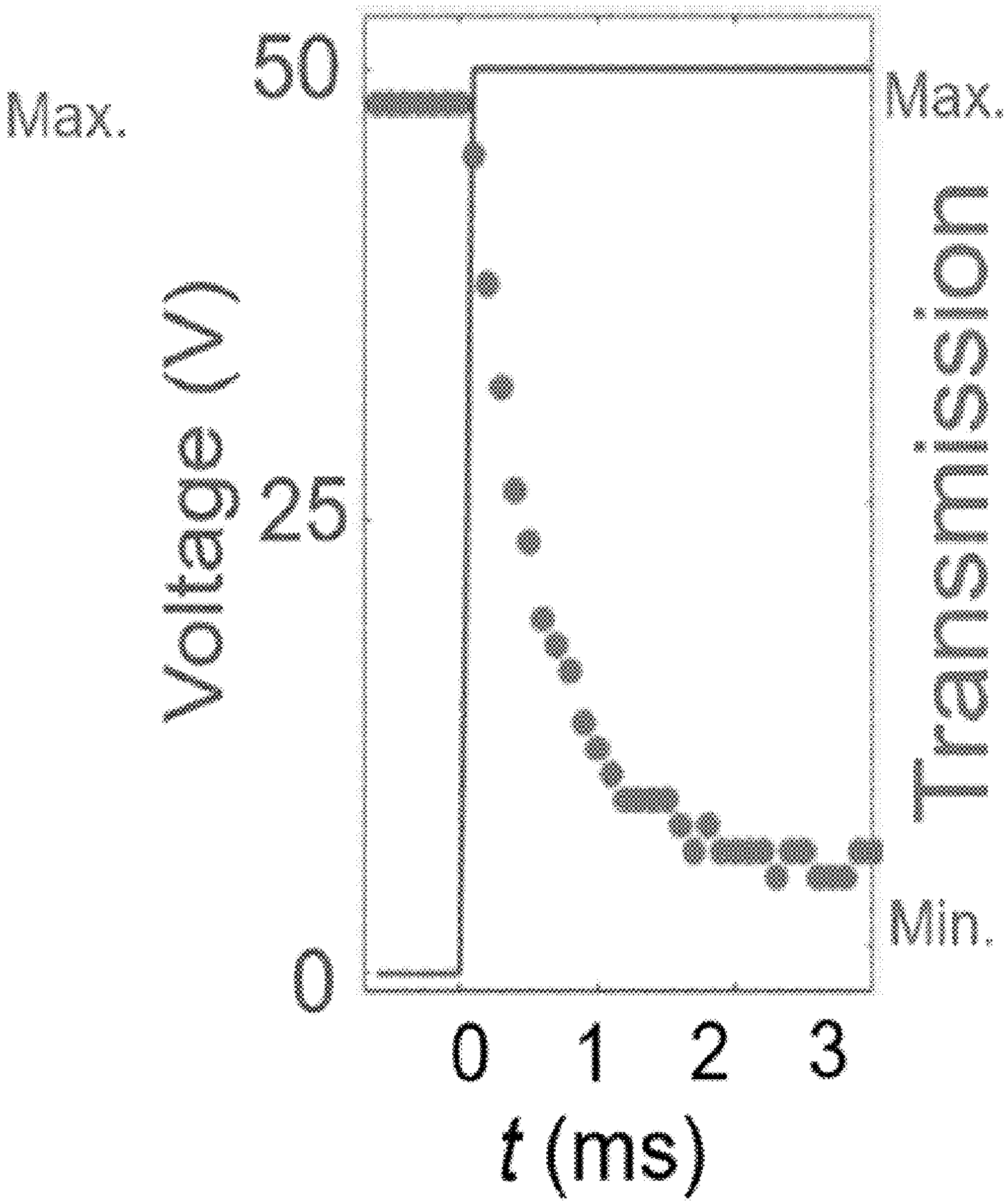


FIG. 5

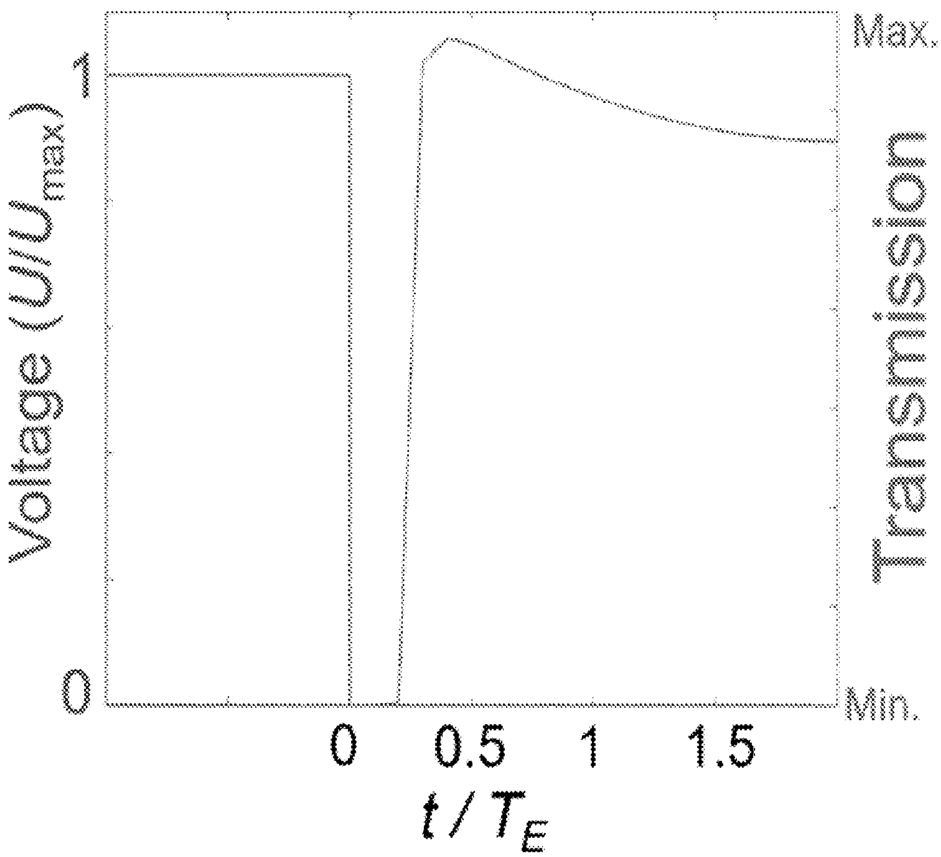


FIG. 6

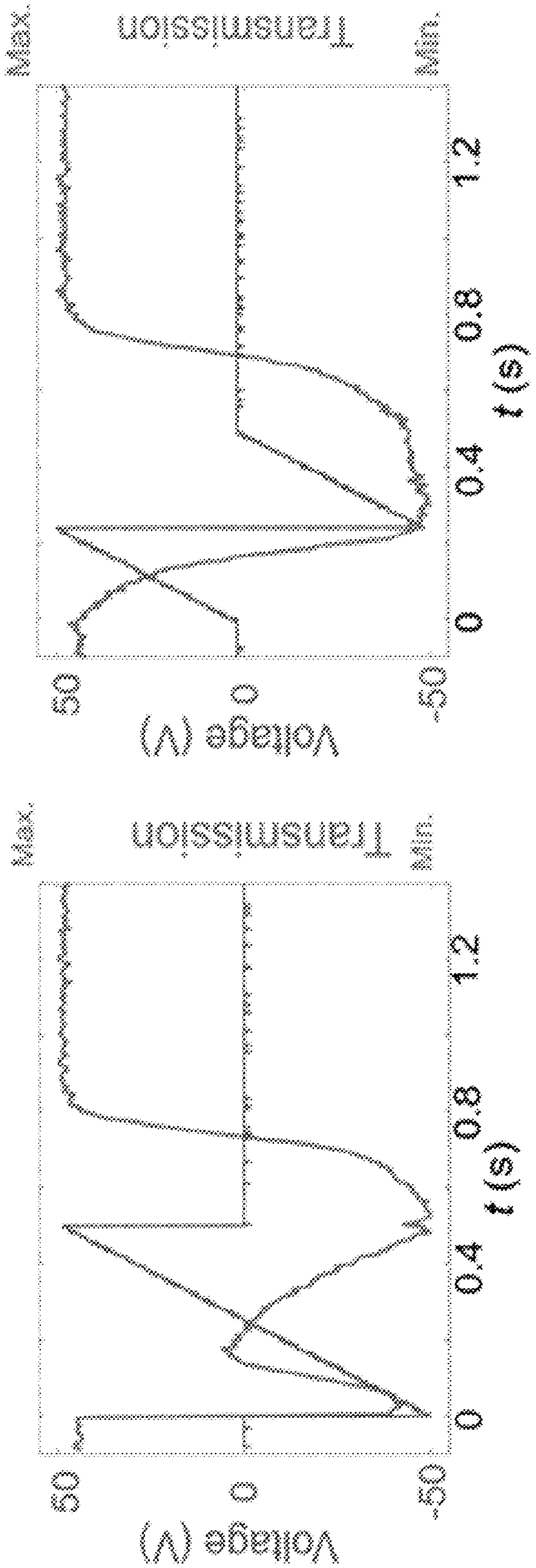
Max.
Transmission
Min.
50
0
-50
Voltage (V)
0
0.4
0.8
1.2
t (s)
Max.
Transmission
Min.
50
0
-50
Voltage (V)
0
0.4
0.8
1.2
t (s)

FIG. 7

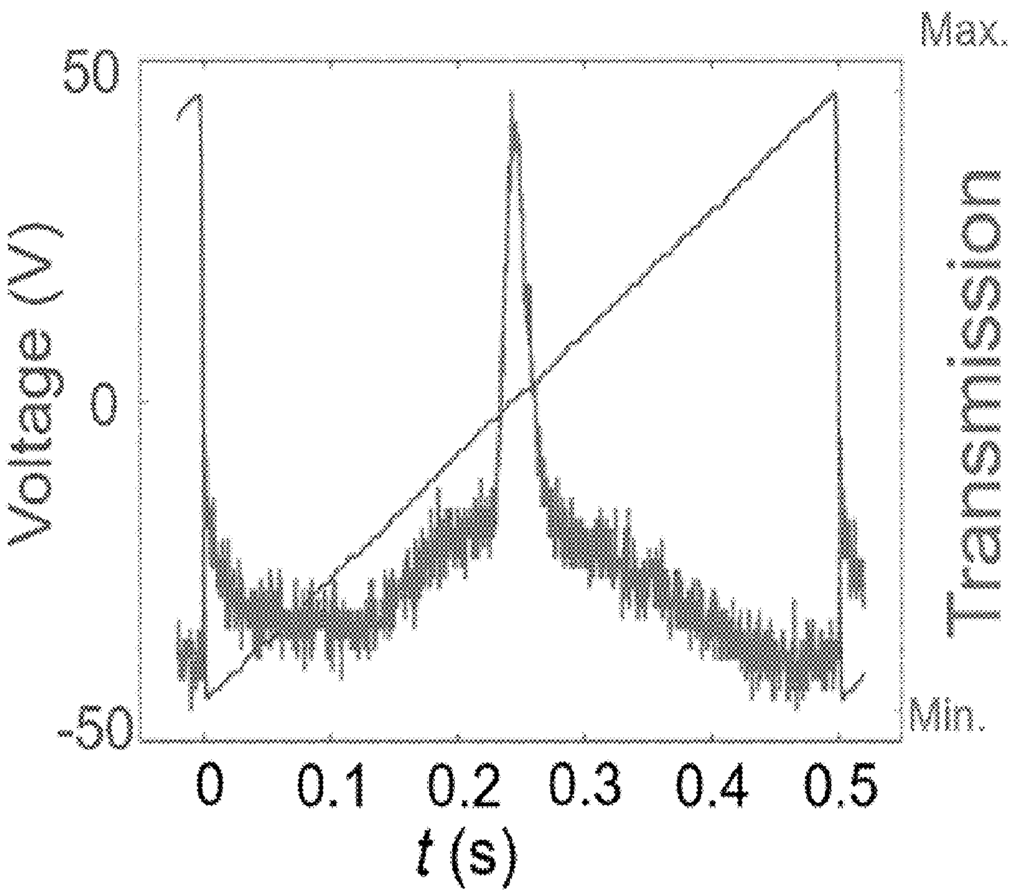


FIG. 8

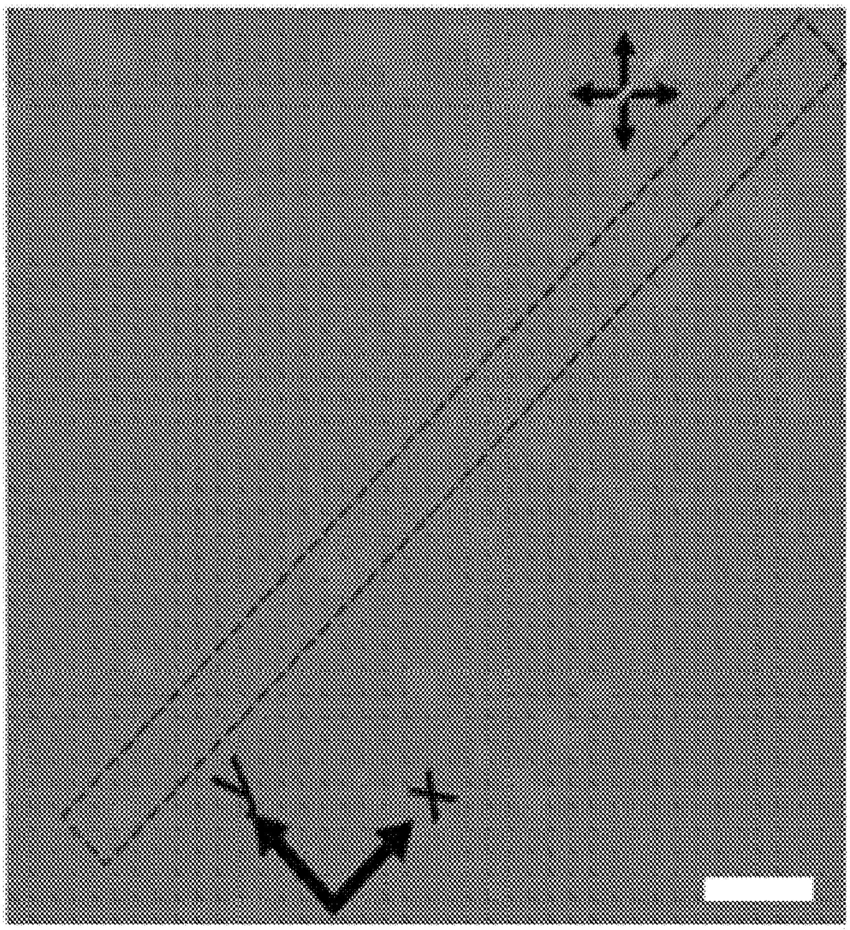


FIG. 9

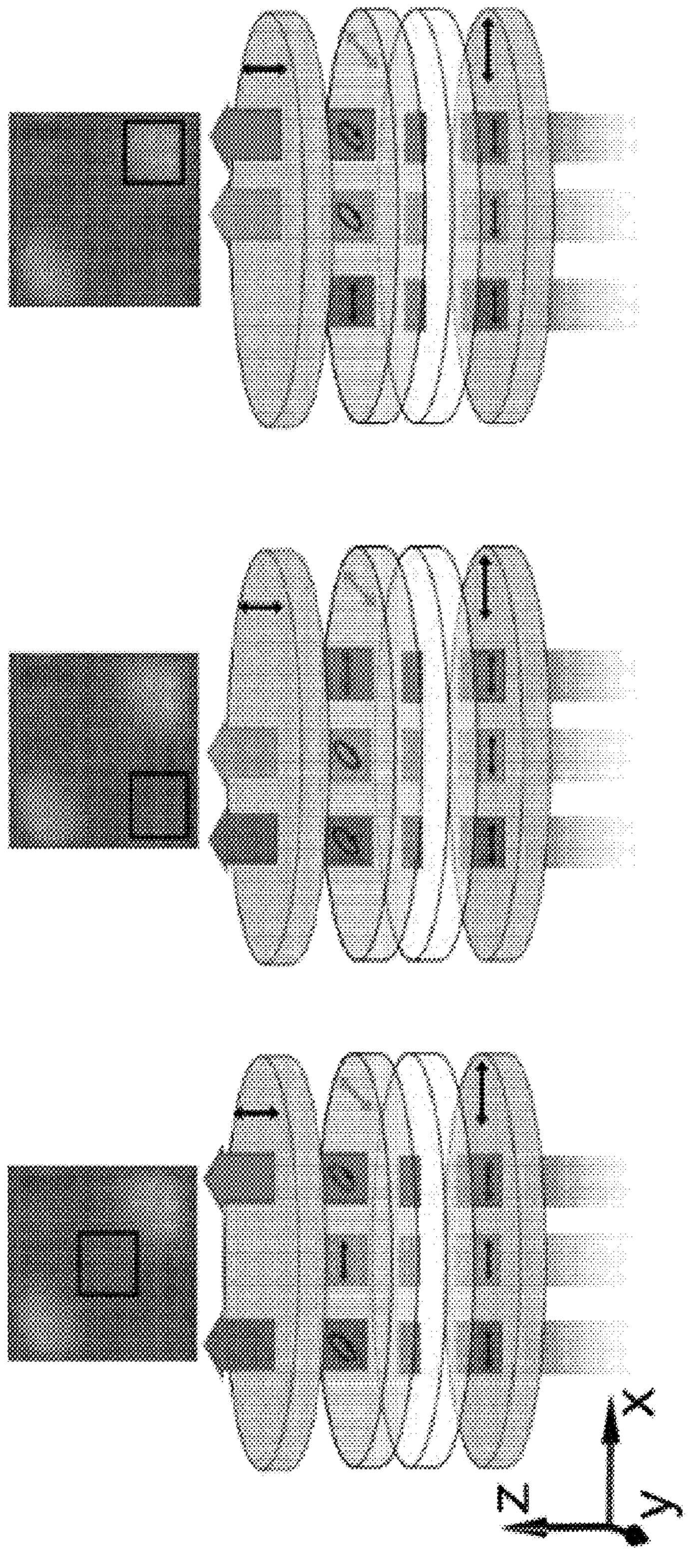


FIG. 10

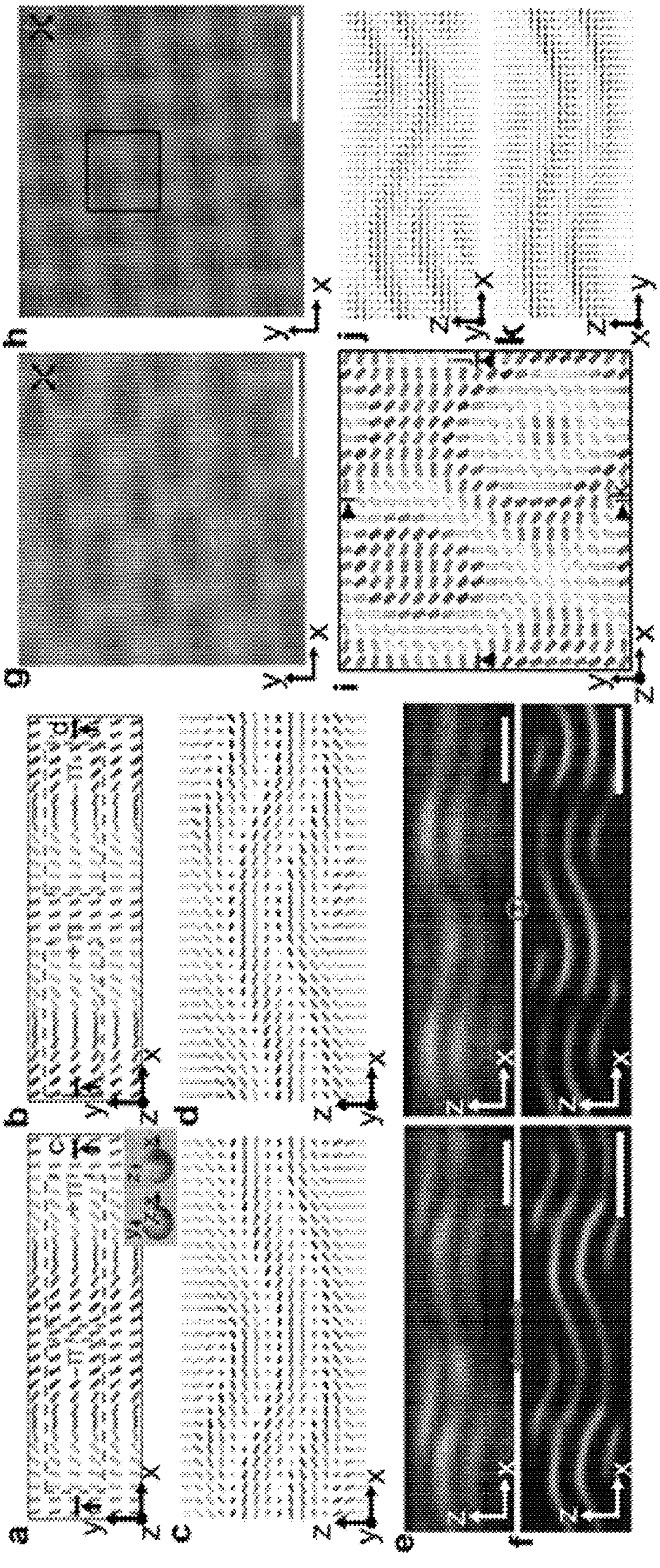

FIG. 11

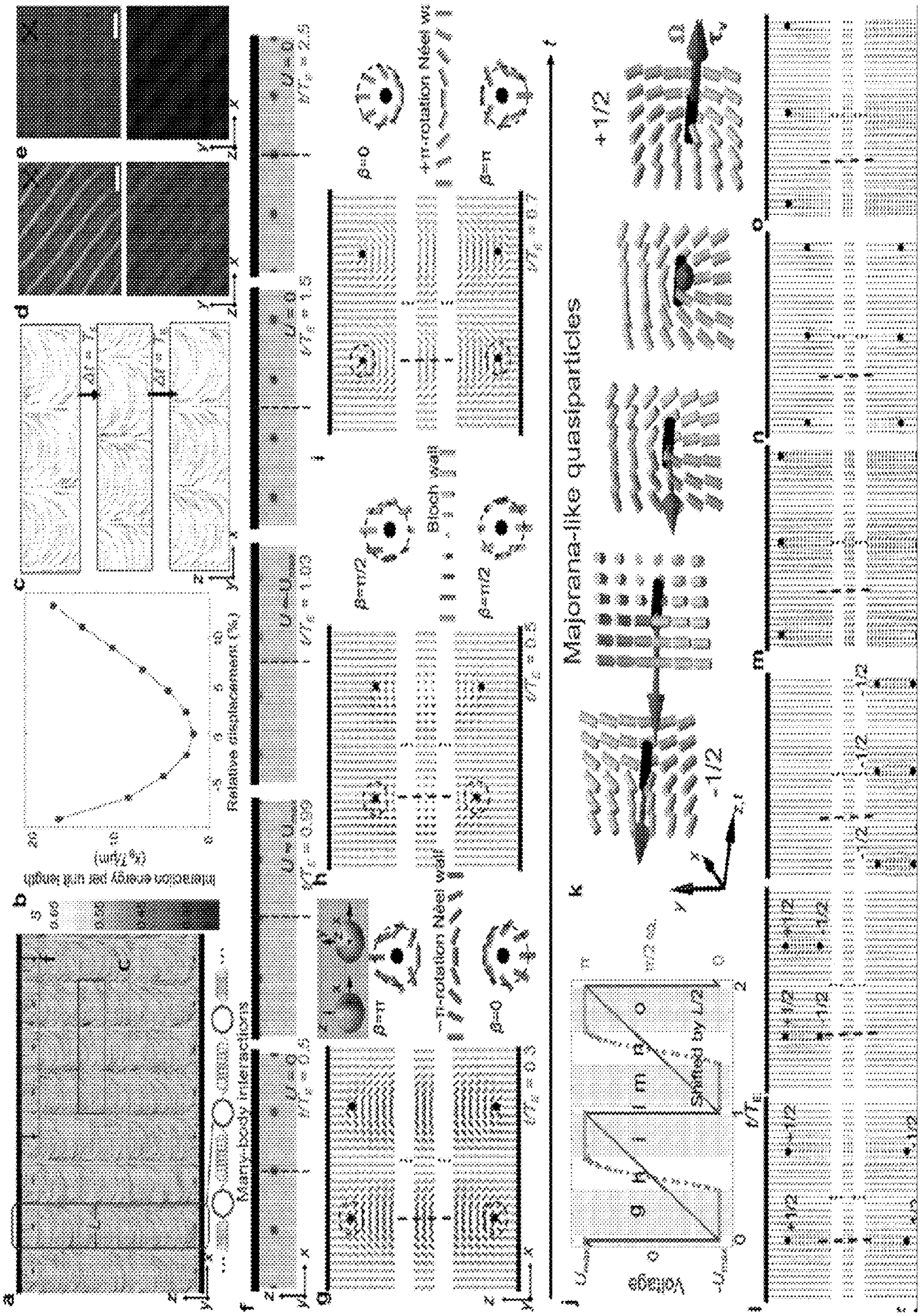
Majorana-like quasiparticles
Many-body interactions
Bloch wall
Relative displacement (%)
Voltage
+1/2
-1/2

FIG. 12

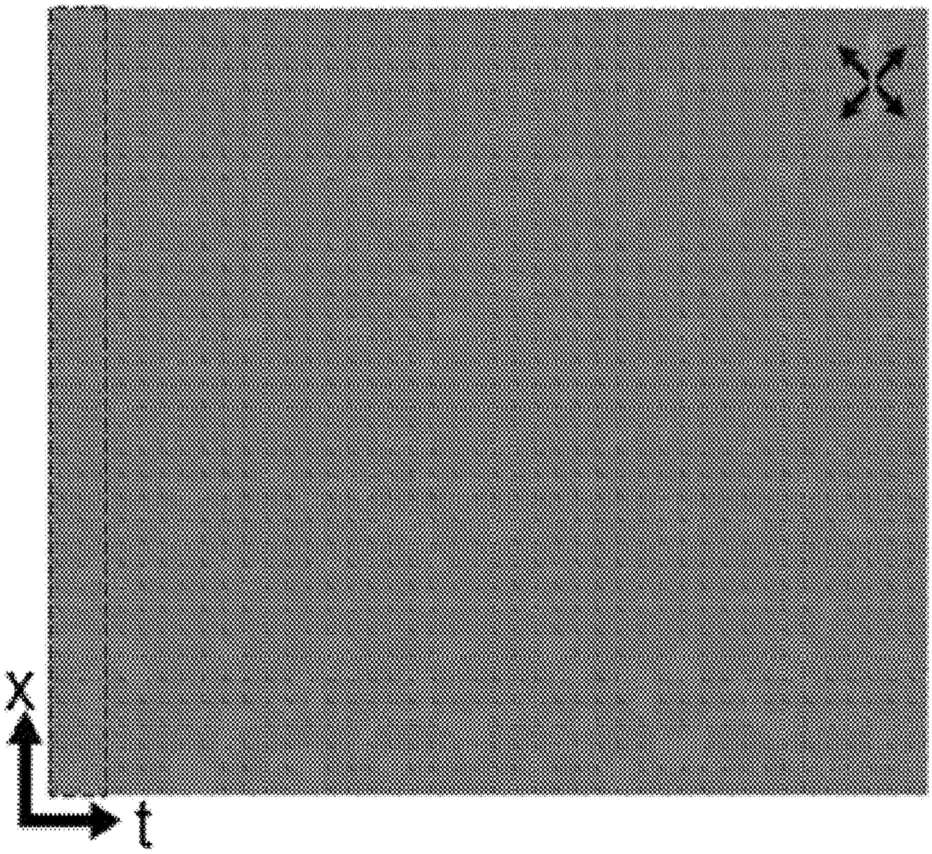


FIG. 13

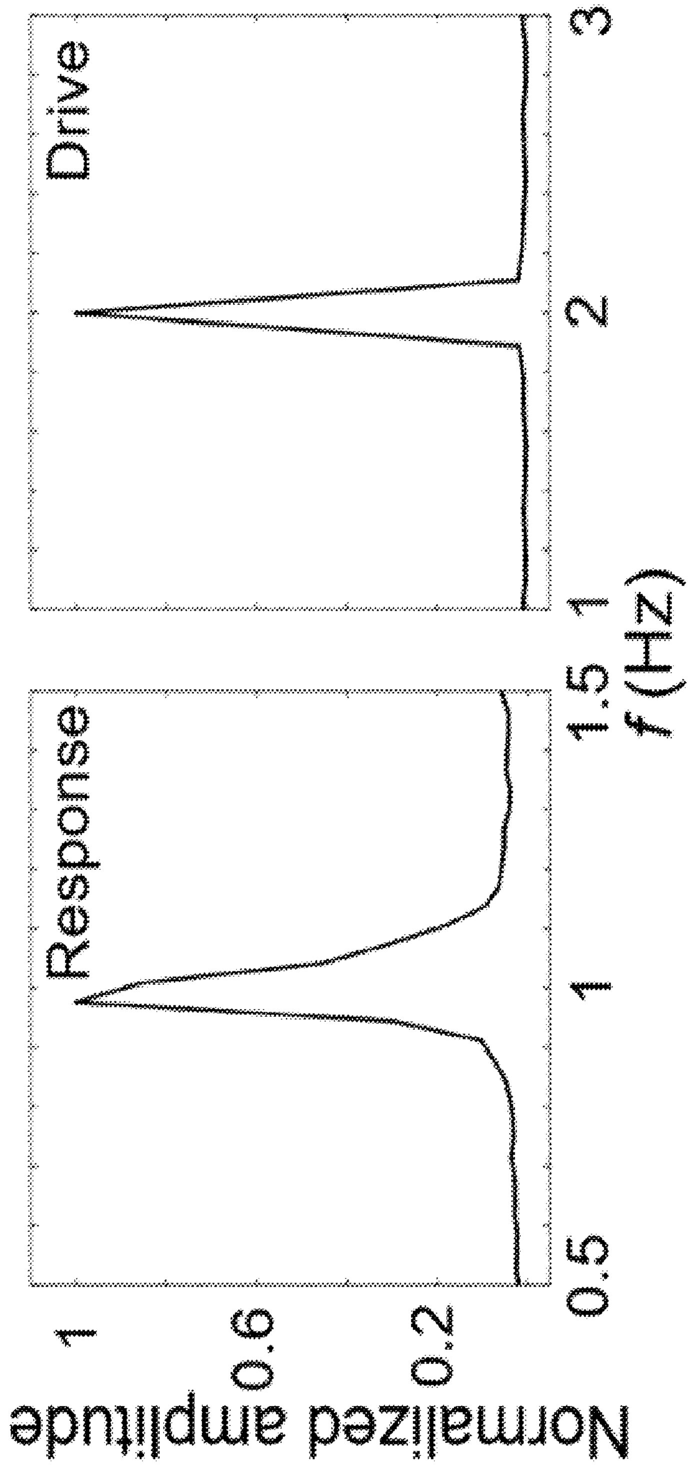


FIG. 14

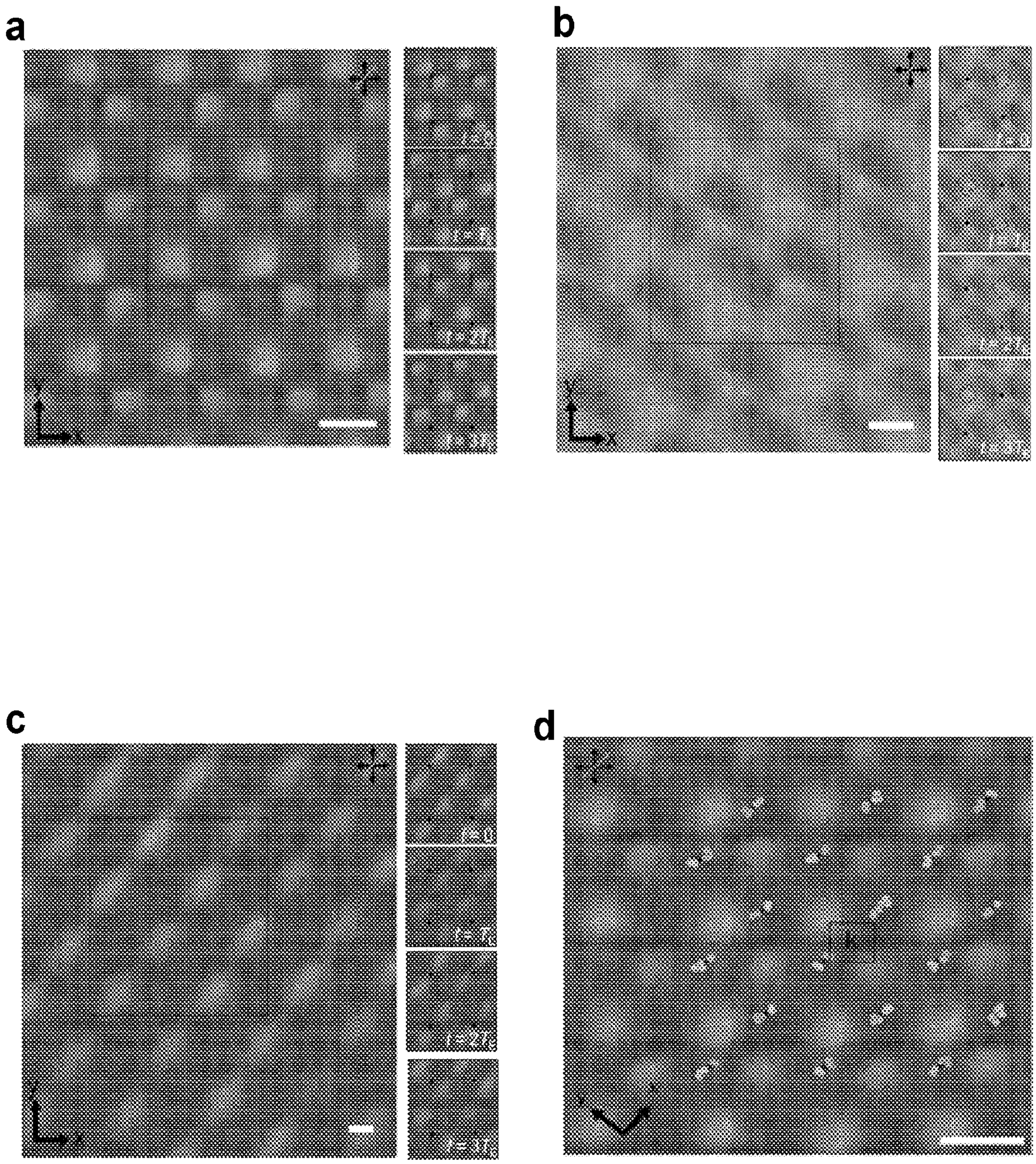


FIG. 15

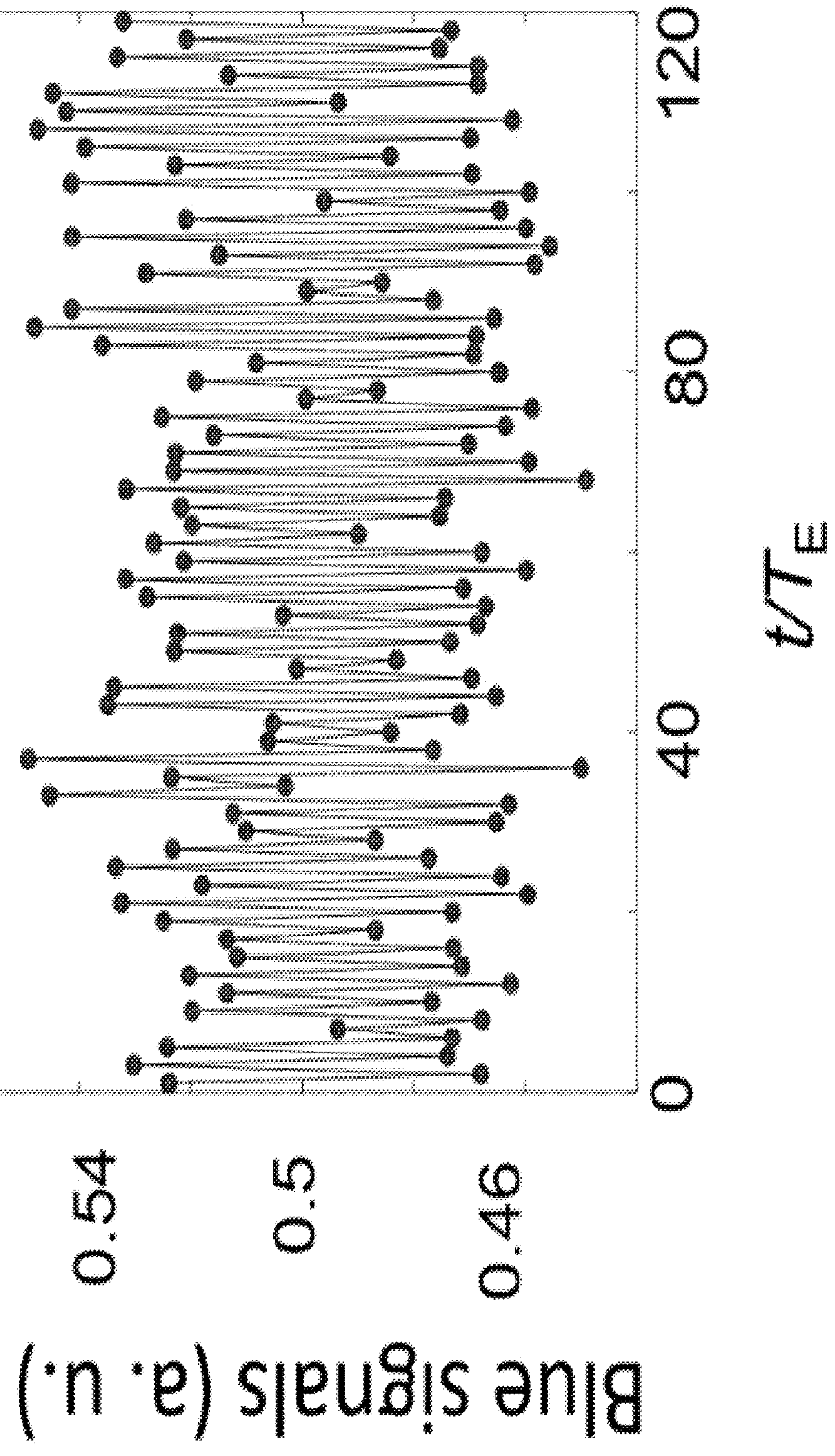


FIG. 16

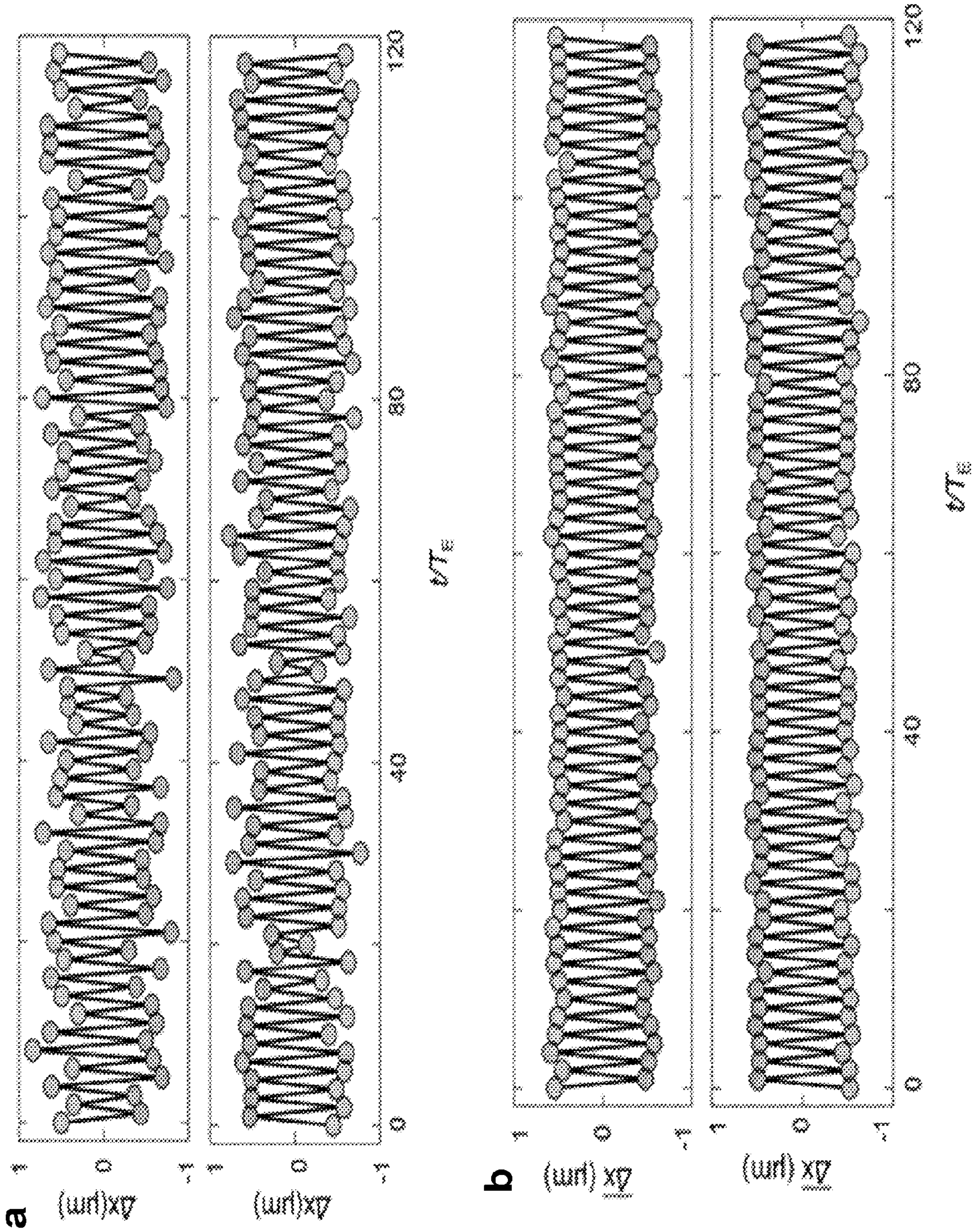


FIG. 17

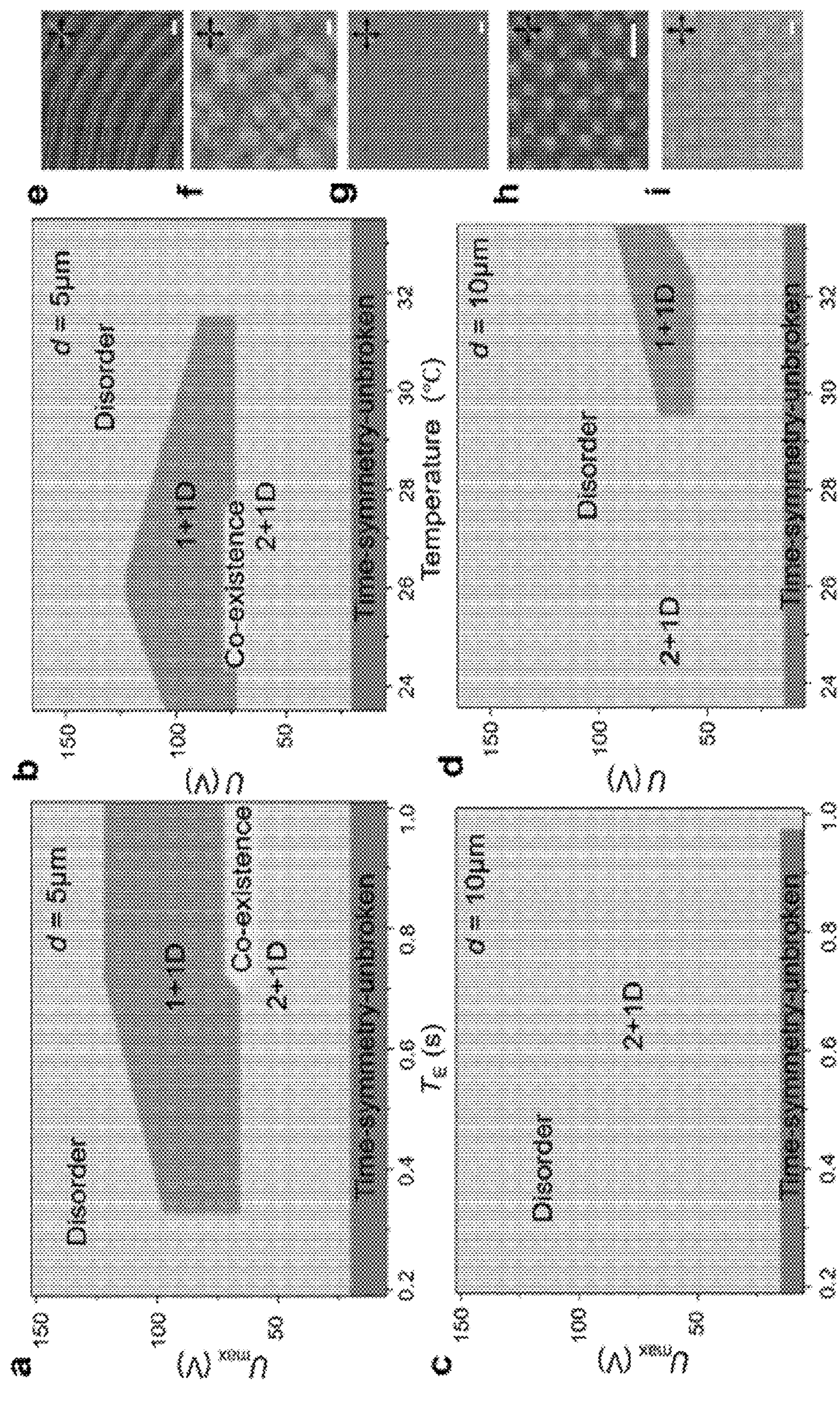
a
b
c
d
e
f
g
h
i
Disorder
1+1D
Co-existence
2+1D
Time-symmetry-unbroken
d = 5μm
d = 10μm
U (V)
Temperature (°C)
24
26
28
30
32
150
100
50
0.2
0.4
0.6
0.8
1.0

FIG. 18

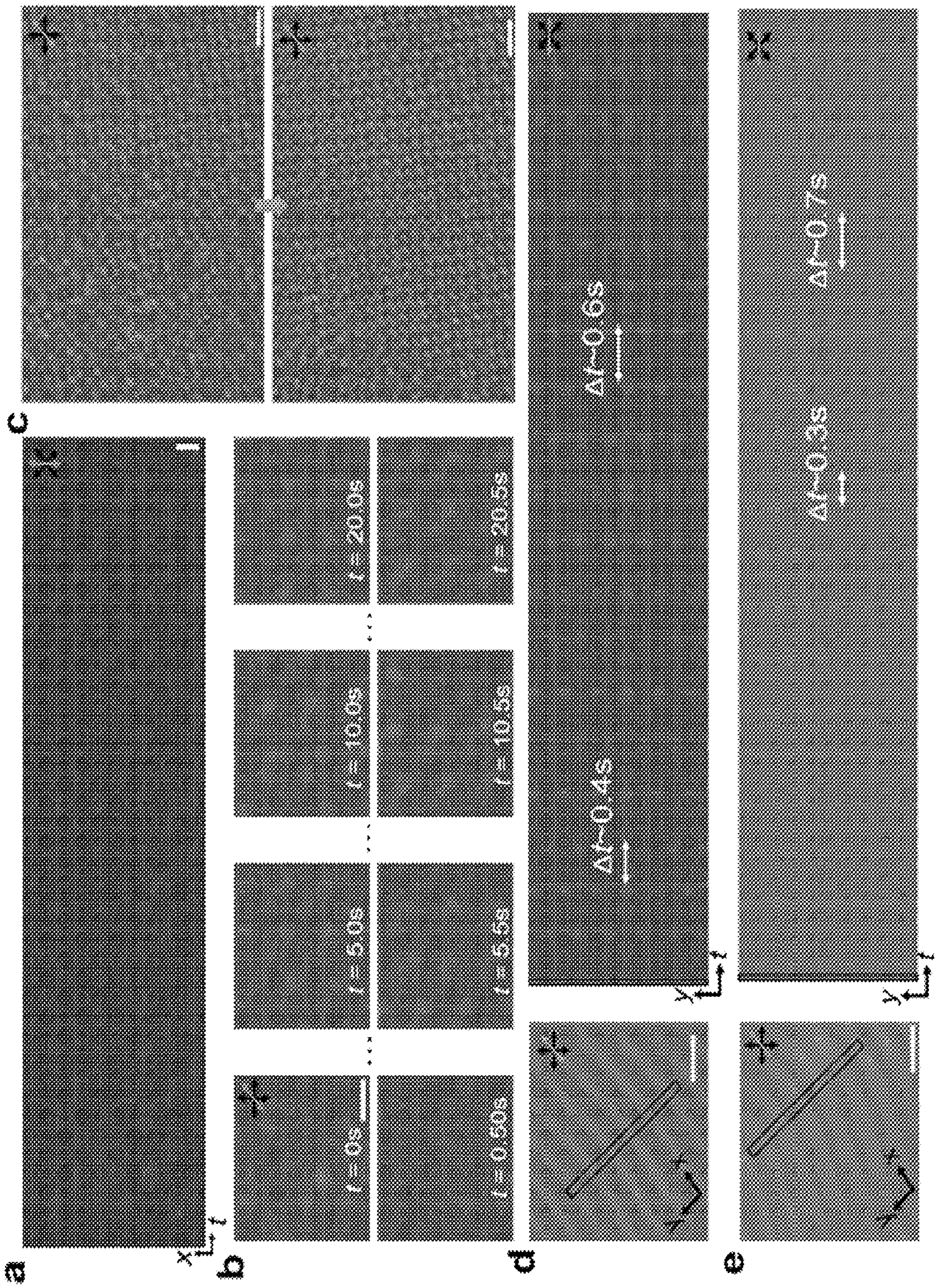
a
b
c
d
e
t = 0s
t = 5.0s
t = 10.0s
t = 20.0s
t = 0.50s
t = 5.5s
t = 10.5s
t = 20.5s
Δt~0.4s
Δt~0.6s
Δt~0.3s
Δt~0.7s

FIG. 19

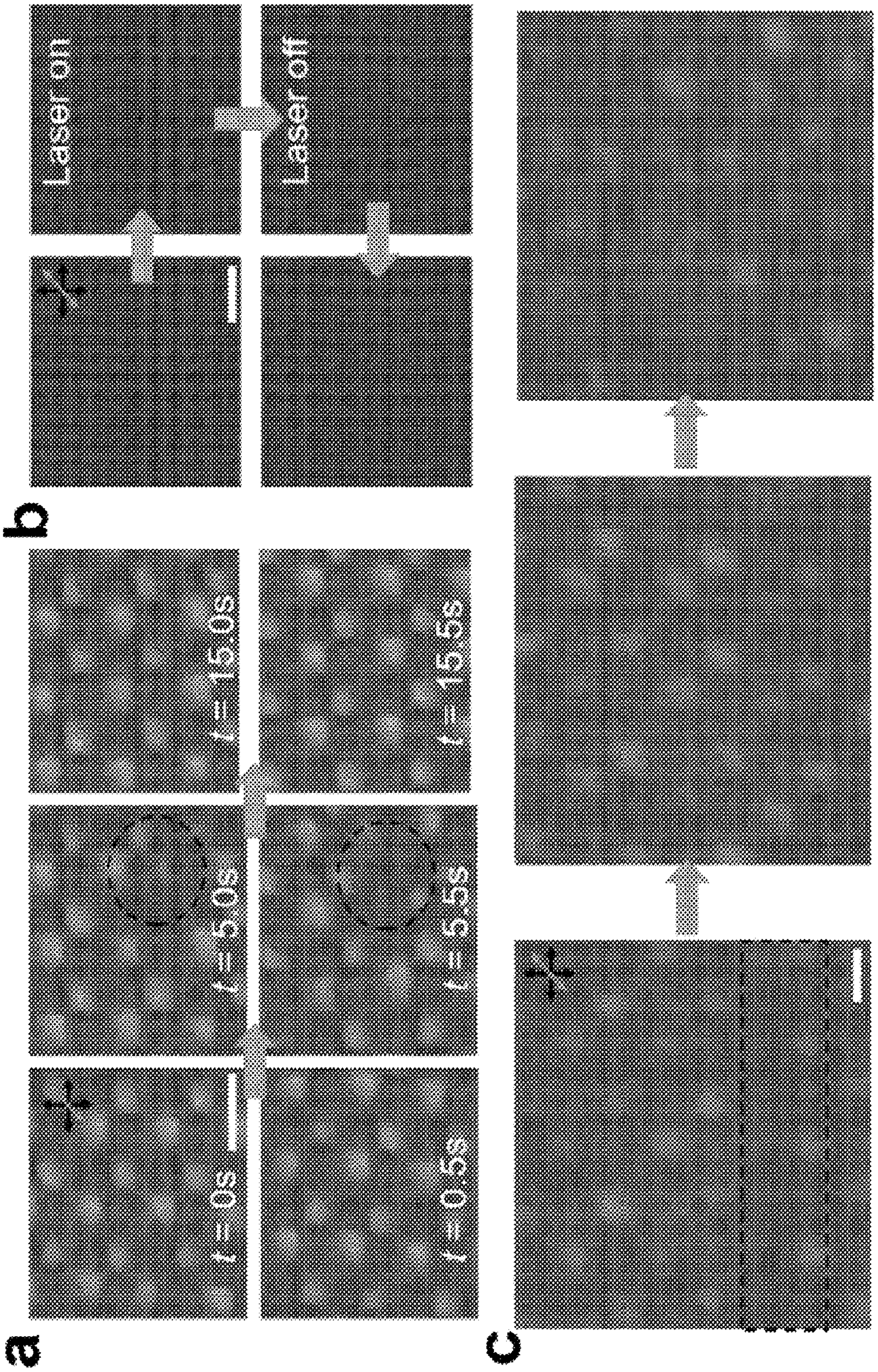


FIG. 20

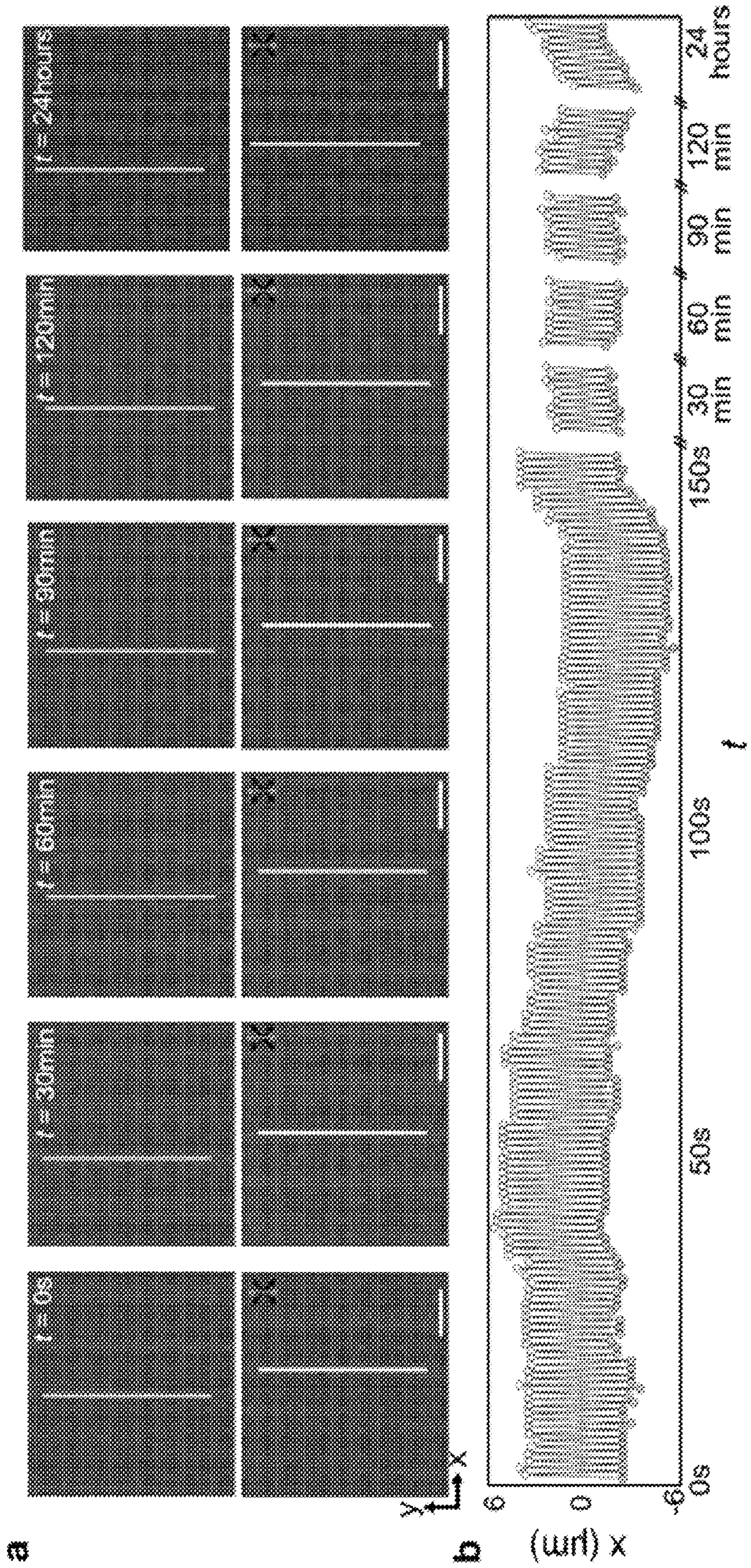
a
b
t = 0s
t = 30min
t = 60min
t = 90min
t = 120min
t = 24hours
y
x
x (μm)
6
0
-6
0s
50s
100s
150s
30 min
60 min
90 min
120 min
24 hours
t

FIG. 21

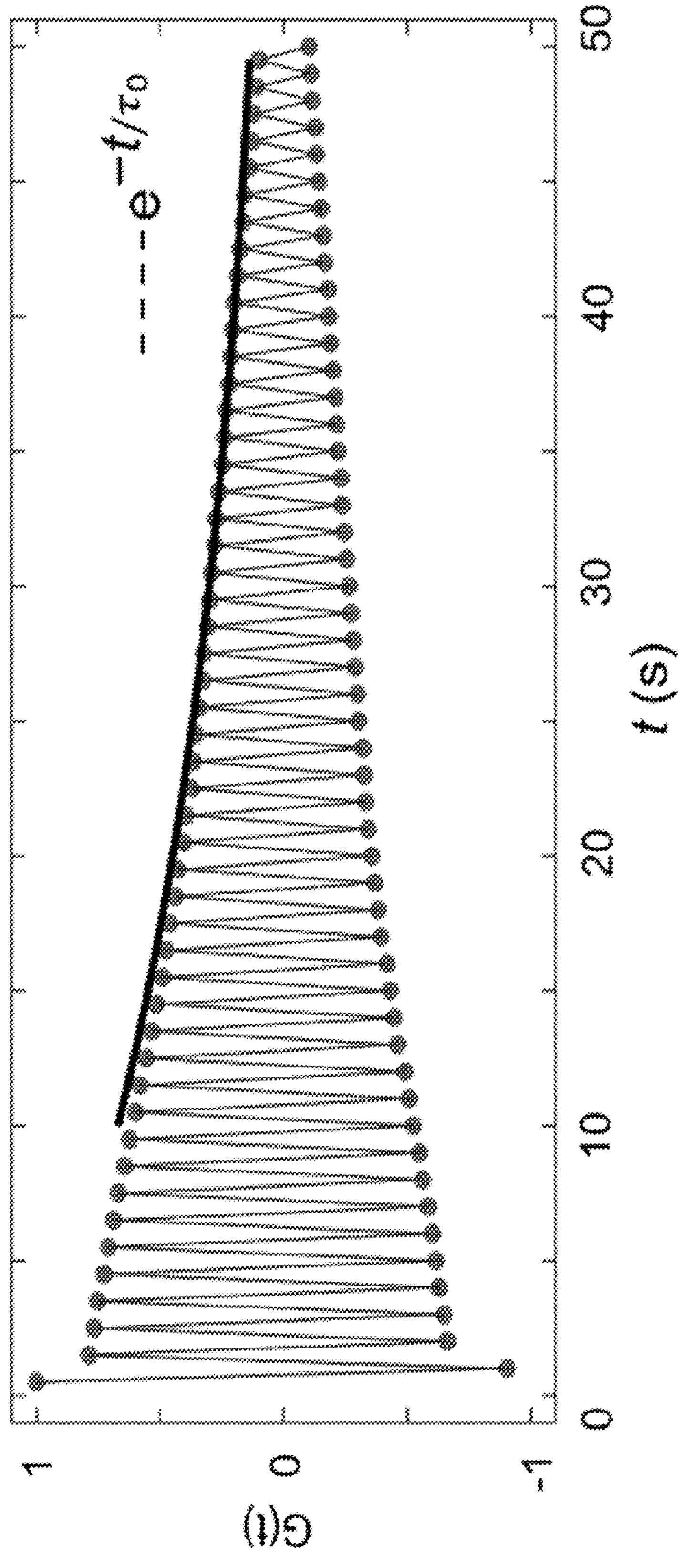


FIG. 22

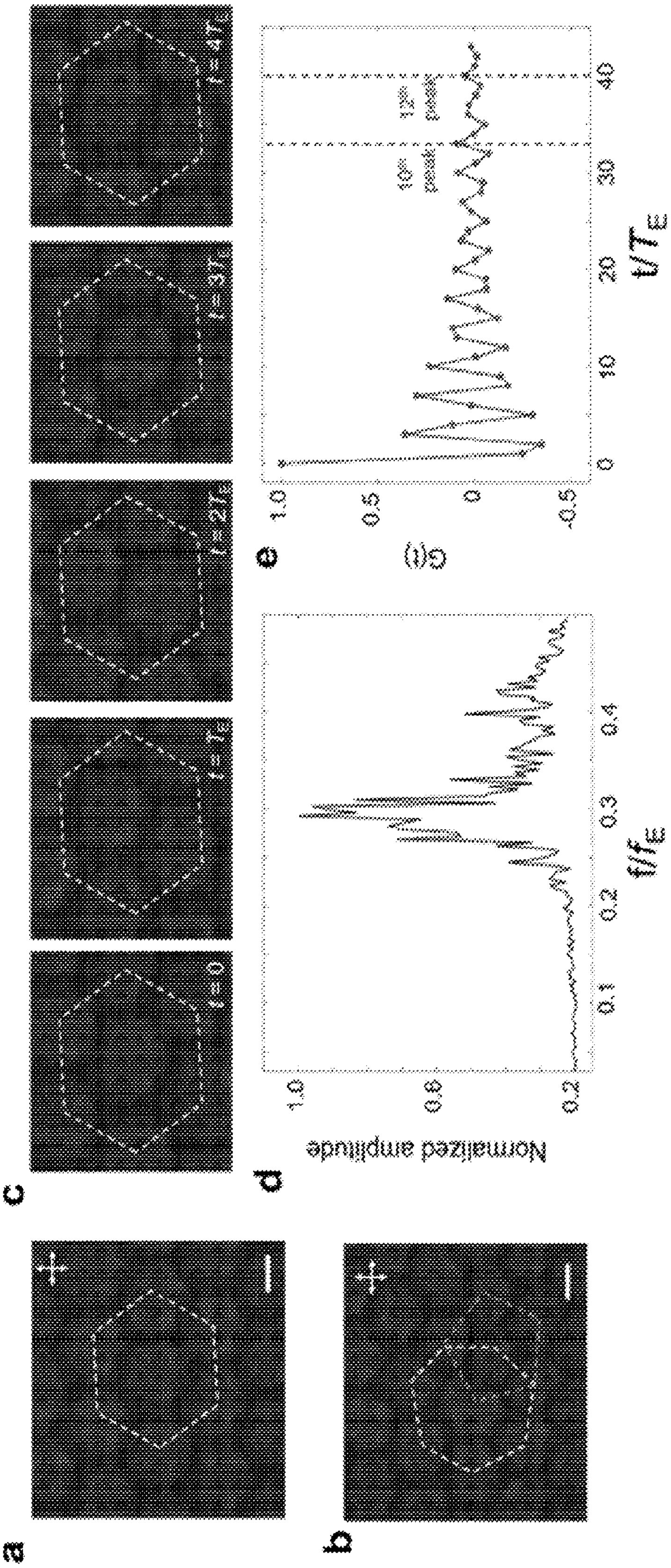


FIG. 23

**INTERNATIONAL SEARCH REPORT**

International application No.

**PCT/US2026/015252**

**A. CLASSIFICATION OF SUBJECT MATTER**

IPC: ***C09K 19/58*** (2026.01); ***C09K 19/02*** (2026.01); ***G02F 1/133*** (2026.01); ***G02F 1/29*** (2026.01); *G02F 1/135* (2026.01)

CPC: ***C09K 19/586; C09K 19/02; G02F 1/133; G02F 1/29;*** *G02F 1/1357*

According to International Patent Classification (IPC) or to both national classification and IPC

**B. FIELDS SEARCHED**

Minimum documentation searched (classification system followed by classification symbols)

See Search History Document

Documentation searched other than minimum documentation to the extent that such documents are included in the fields searched

See Search History Document

Electronic data base consulted during the international search (name of data base and, where practicable, search terms used)

See Search History Document

**C. DOCUMENTS CONSIDERED TO BE RELEVANT**

| Category* | Citation of document, with indication, where appropriate, of the relevant passages | Relevant to claim No. |
|---|---|---|
| Y | US 2012/0013574 A1 (Murai et al.) 19 January 2012 (19.01.2012)<br>abstract, [0018], [0027], [0075], [0163]-[0164] | 1-9, 17-20/(1-9) |
| A | US 2020/0183202 A1 (BOE Technology Group Co., Ltd. ) 11 June 2020 (11.06.2020)<br>entire document | 1-9, 17-20/(1-9) |
| A | US 2022/0025267 A1 (Zymergen Inc.) 27 January 2022 (27.01.2022)<br>entire document | 1-9, 17-20/(1-9) |
| Y | Xie et al., "Liquid Crystal Droplet-Based Biosensors: Promising for Point-of-Care Testing", 15 September 2022, Biosensors 2022, 12, 758. https://doi.org/10.3390/bios12090758<br>abstract, pg 2 para 1 | 1-9, 17-20/(1-9) |
| Y | Zhou et al., "Cavity Floquet engineering", 06 September 2024, Nat Commun 15, 7782 (2024). https://doi.org/10.1038/s41467-024-52014-0<br>abstract, pg 5 col 1 para 3 | 9, (17-20)/9 |

☑ Further documents are listed in the continuation of Box C.

☐ See patent family annex.

* Special categories of cited documents:

"A" document defining the general state of the art which is not considered to be of particular relevance

"D" document cited by the applicant in the international application

"E" earlier application or patent but published on or after the international filing date

"L" document which may throw doubts on priority claim(s) or which is cited to establish the publication date of another citation or other special reason (as specified)

"O" document referring to an oral disclosure, use, exhibition or other means

"P" document published prior to the international filing date but later than the priority date claimed

"T" later document published after the international filing date or priority date and not in conflict with the application but cited to understand the principle or theory underlying the invention

"X" document of particular relevance; the claimed invention cannot be considered novel or cannot be considered to involve an inventive step when the document is taken alone

"Y" document of particular relevance; the claimed invention cannot be considered to involve an inventive step when the document is combined with one or more other such documents, such combination being obvious to a person skilled in the art

"&" document member of the same patent family

| Date of the actual completion of the international search | Date of mailing of the international search report |
|---|---|
| **12 April 2026 (12.04.2026)** | **10 June 2026 (10.06.2026)** |

| Name and mailing address of the ISA/US | Authorized officer |
|---|---|
| **COMMISSIONER FOR PATENTS<br>MAIL STOP PCT, ATTN: ISA/US<br>P.O. Box 1450<br>Alexandria, VA 22313-1450<br>UNITED STATES OF AMERICA** | **HARRY KIM** |
| Facsimile No. **571-273-8300** | Telephone No. **PCT Help Desk: 571-272-4300** |

| C. DOCUMENTS CONSIDERED TO BE RELEVANT | | |
|---|---|---|
| Category* | Citation of document, with indication, where appropriate, of the relevant passages | Relevant to claim No. |
| Y | Zhan et al., “Pancharatnam-Berry optical elements for head-up and near-eye displays”, 22 February 2019, Vol. 36, No. 5 / May 2019 / Journal of the Optical Society of America B, https://doi.org/10.1364/JOSAB.36.000D52<br>abstract, D52 col 1 para 5- col 2 para 1 | 17-18 |

**Box No. III Observations where unity of invention is lacking (Continuation of item 3 of first sheet)**

This International Searching Authority found multiple inventions in this international application, as follows:

This application contains the following inventions or groups of inventions which are not so linked as to form a single general inventive concept under PCT Rule 13.1.

Group I: Claims 1-9, (17-20)(in part), directed to a device comprising a power supply configured to apply an applied signal having a first period, wherein, in response to the applied signal, a period of an optical signal of light emitted from the device is an integer multiple of the first period.

Group II: Claims 10-16, (17-20)(in part), directed to a device comprising a power supply configured to apply an applied signal having a first period, wherein the doped chiral nematic liquid crystal material comprises discrete space-time crystals.

1. ☐ As all required additional search fees were timely paid by the applicant, this international search report covers all searchable claims.

2. ☐ As all searchable claims could be searched without effort justifying additional fees, this Authority did not invite payment of additional fees.

3. ☐ As only some of the required additional search fees were timely paid by the applicant, this international search report covers only those claims for which fees were paid, specifically claims Nos.:

4. ☑ No required additional search fees were timely paid by the applicant. Consequently, this international search report is restricted to the invention first mentioned in the claims; it is covered by claims Nos.: **1-9, (17-20)(in part)**

**Remark on Protest**

☐ The additional search fees were accompanied by the applicant's protest and, where applicable, the payment of a protest fee.

☐ The additional search fees were accompanied by the applicant's protest but the applicable protest fee was not paid within the time limit specified in the invitation.

☐ No protest accompanied the payment of additional search fees.